Multiresolution angular momentum measurements of $z \sim 1.5-2$ star-forming galaxies

Juan M. Espejo Salcedo [1]★ Karl Glazebrook,[1] Deanne B. Fisher [1] Sarah M. Sweet,[2,3]
Danail Obreschkow [4] A. M. Swinbank [5] Steven Gillman [5,6,7] and Alfred L. Tiley[4]

[1]*Centre for Astrophysics & Supercomputing, Swinburne University of Technology, PO Box 218, Hawthorn, VIC 3122, Australia*
[2]*School of Mathematics and Physics, University of Queensland, Brisbane, QLD 4072, Australia*
[3]*ARC Centre of Excellence for All Sky Astrophysics in 3 Dimensions (ASTRO 3D)*
[4]*International Centre for Radio Astronomy Research, University of Western Australia, 7 fairway, Crawley, WA 6009, Australia*
[5]*Centre for Extra-galactic Astronomy, Durham University, South Road, Durham DH1 3LE, UK*
[6]*Cosmic Dawn Centre (DAWN), DK-2200 Copenhagen, Denmark*
[7]*DTU-Space, Technical University of Denmark, Elektrovej 327, DK-2800 Kgs. Lyngby, Denmark*

ABSTRACT

We present detailed stellar specific angular momentum (j_*) measurements of 10 star-forming galaxies at $z \sim 1.5-2$, using both high and low spatial resolution integral field spectroscopic data. We developed a code that simultaneously models the adaptive optics (AO) assisted observations from OSIRIS/SINFONI along with their natural seeing (NS) counterparts from KMOS at spatial resolutions of [0.1−0.4] arcsec and [0.6−1.0] arcsec, respectively. The AO data reveal 2/10 systems to be mergers and for the remaining eight the mean uncertainties $\bar{\Delta} j_*$ decrease from 49 per cent (NS), and 26.5 per cent (AO), to 16 per cent in the combined analysis. These j_* measurements agree within 20 per cent with simple estimates ($\tilde{j}_*$) calculated from *Hubble Space Telescope* photometry and NS kinematics; however, higher resolution kinematics are required to first identify these discs. We find that the choice of surface mass density model and the measurement of effective radius from photometry are the key sources of systematic effects in the measurement of j_* between different analyses. Fitting the j_* versus M_* relations (Fall 1983) with a fixed power-law slope of $\beta = 2/3$, we find a zero-point consistent with prior NS results at $z \geq 1$ within ~ 0.3 dex. Finally, we find a ~ 0.38 dex scatter about that relation that remains high despite the AO data so we conclude it is intrinsic to galaxies at $z > 1$. This compares to a scatter of ≤ 0.2 dex for discs at $z \simeq 0$ pointing to a settling of the Fall relation with cosmic time.

Key words: Galaxies: discs – galaxies: evolution – galaxies: kinematics and dynamics.

1 INTRODUCTION

Approximately half of all the stars in the Universe were formed during the time period when it was 3–6 Gyr old ($1 < z < 3$), with the peak of star formation happening at around $z \sim 2$ (Madau & Dickinson 2014). At this epoch, the majority of the galaxy population appears very different from the rapidly rotating discs that make up the bulk of the star-forming galaxies in the local Universe. At $z \sim 2$, star-forming galaxies had clumpy morphologies (Glazebrook et al. 1995; Conselice, Bershady & Jangren 2000; Elmegreen et al. 2005; Livermore et al. 2015), their gas fractions (f_{gas}) were high compared to local analogues (Bouché et al. 2007; Tacconi et al. 2013; Decarli et al. 2019) and for a fixed stellar mass (M_*), their stellar specific angular momentum $j_* = J_*/M_*$ was lower than that of local discs (Law et al. 2009; Obreschkow et al. 2015; Teklu et al. 2015).

The morphological diversity of regular galaxies at low redshift, typically classified by the Hubble sequence (Hubble 1926), emerged at $z \sim 2$ (Szomoru et al. 2011), where the transition from the high-redshift turbulent discs to the grand design spirals we observe in the local Universe begins to take place. Both observations and theoretical

models suggest that galaxy-wide instabilities play an important role in driving the evolution of galaxies during this epoch (Genzel et al. 2008; Dekel, Sari & Ceverino 2009; Dekel & Burkert 2014; Tacchella et al. 2016). These strong instabilities can be produced in major merger events and gravitational interactions that are more frequent at $z > 1.5$ (Ventou et al. 2017, 2019). In the absence of mergers, a galaxy-wide instability in a rotating system can be generated by a combination of high gas surface density and low angular momentum.

Angular momentum is a fundamental physical quantity that sets the disc size and thickness and induces scaling relations such as the Fundamental Plane of spiral galaxies and the Tully–Fisher relation (Tully & Fisher 1977). It provides an alternative to the Hubble-type morphological classification (Fall & Efstathiou 1980; van den Bosch 1998; Obreschkow & Glazebrook 2014) and drives the dynamical evolution of a galaxy throughout its history.

In the current framework for galaxy formation, self-bound structures of non-baryonic matter assemble due to gravitational collapse to form dark matter haloes (Peebles 1969; Blumenthal et al. 1984; Wechsler & Tinker 2018). These protohaloes acquire angular momentum as a result of tidal torques from the random alignment and orientation of the large-scale environment (Mo, Mao & White 1998; Liao et al. 2017). The acquired specific angular momentum of the halo (j_h) has a halo mass (M_h) dependence of the form $j_h \propto M_h^{2/3}$

★ E-mail: jespejosalcedo@swin.edu.au

(Catelan & Theuns 1996a; Catelan & Theuns 1996b). As the gas cools and collapses to the centre of the dark matter halo, a rotationally supported disc is formed. Baryonic angular momentum is distributed within the disc by local torques and stellar feedback. In the case of star-forming disc galaxies (and in the absence of major mergers), the stellar specific angular momentum approximately preserves the halo dynamical properties and scales with the stellar mass as $j_* \propto M_*^{2/3}$ (Romanowsky & Fall 2012; Harrison et al. 2017; Fall & Romanowsky 2018; Posti et al. 2018).

Stellar specific angular momentum is expected to increase with cosmic time as $j_* \propto (1 + z)^{-n}$ with $n \sim 0.5-1$ (e.g. Obreschkow et al. 2015 from theoretical predictions and Swinbank et al. 2017 from observations). The power-law slope, n, may vary as angular momentum is redistributed due to star formation feedback, outflows, and winds (Naab & Ostriker 2017). Empirically constraining the angular momentum evolution is key in reproducing galaxies with realistic morphology, rotation, and size in cosmological hydrodynamical simulations (Pichon et al. 2011; Teklu et al. 2015).

Galaxy angular momentum is therefore a fundamental quantity that is not directly observed but derived from kinematics and stellar mass distributions. At high redshift, this is particularly difficult, one needs to both resolve the steep rising part of the rotation curve as well as the flat outer end to derive rotation profiles.

The majority of the current kinematic measurements at high-redshift come from seeing limited observations (SINS; Förster Schreiber et al. 2009, KMOS³D; Wisnioski et al. 2015, KROSS; Swinbank et al. 2017, KGES; Gillman et al. 2020). These measurements are heavily affected by beam smearing, leading to degraded spatial resolutions of ~8 kpc and due to the possible misclassification of mergers and disks (Bellocchi, Arribas & Colina 2012; Epinat et al. 2012; Rodrigues et al. 2017; Simons et al. 2019; Sweet et al. 2019).

Adaptive optics assisted observations are required to resolve the inner part of the rotation curves since they improve resolution (at the ~1 kpc level which is comparable to galaxy r_{eff} values) but are typically limited to a smaller field of view and have a lower throughput than seeing limited observations (Burkert et al. 2016; Gillman et al. 2019). One way to account for this is to combine data at different resolutions as suggested in Glazebrook (2013) and implemented by Obreschkow et al. (2015) who made a combined analysis of galaxies at $z \sim 0$ with both low- and high-resolution data. Currently, despite the large amounts of seeing limited measurements at $z \sim 1-2$, only a small number overlap with adaptive optics observations so any combined measurement of j_* is limited to a small number of galaxies (e.g. Sweet et al. 2019 with two galaxies at $z \sim 1.5$).

In this paper, we implement a combined measurement of the dynamics of ten star-forming galaxies to investigate the systematics in the existing measurements from seeing-limited surveys. In Section 2, we present the details of our kinematic and photometric sample. We describe the methods used to measure the dynamical properties, the PSF modelling and the combination of the different data sets in Section 3. In Section 4, we discuss the enhanced angular momentum measurements and the capabilities of our modelling, and in Section 5, we present the results and conclusions of the paper. We include an appendix describing the kinematic fitting code and the different sanity checks used to avoid systematics, as well as a supplementary (online) section with an additional appendix describing each galaxy individually. Throughout the paper we assume a ΛCDM cosmology with $\Omega_m = 0.3$, $\Omega_\Lambda = 0.7$, and $H_0 = 70$ km s⁻¹ Mpc⁻¹.

2 OBSERVATIONS AND SAMPLE DESCRIPTION

We analyse a sample of ten galaxies that have adaptive optics 'AO' assisted observations and natural seeing 'NS' limited counterparts. This sample consists of five galaxies at $z \sim 1.5$ from Keck/OSIRIS (AO) + VLT/KMOS (NS) shown in Fig. 1 and five galaxies from VLT/SINFONI (AO) + VLT/KMOS (NS) at $z \sim 2$ shown in Fig. 2. We do not include galaxies at $z < 1.5$ in our analysis due to low Strehl. In this section, we describe the sample selection and the characteristics of the data from integral field spectroscopy, as well as the near-infrared photometric data from *HST*. Table 1 summarizes the instruments used in our full sample and some of the main parameters of the 10 galaxies.

2.1 Sample at $z \sim 1.5$

2.1.1 KGES observations (natural seeing)

We used the reduced datacubes of the galaxies COSMOS 110446, COSMOS 171407, COSMOS 130477, COSMOS 127977, and UDS 78317 from the KMOS Galaxy Evolution Survey (KGES; Tiley et al. 2021). This survey comprises a sample of 288 mass-selected bright ($K < 22.7$) star-forming galaxies with known spectroscopic redshifts at $z \sim 1.5$ in the ECDFS, UDS, and COSMOS fields targeting their redshifted Hα and [NII] emission lines.

The instrument used for this survey is the *K*-band multiobject spectrograph (KMOS; Sharples et al. 2013) at a pixel scale of 0.2 arcsec per pixel. The mean PSF FWHM (point spread function at full width at half maximum) of the KGES sample is ~0.6 arcsec and the spectral resolution is $R \sim 3975$ at the location of Hα emission in the *K* band. These galaxies were chosen based on the ordered rotation that they appeared to have in seeing limited IFS data for the follow-up observations with adaptive optics. The *HST* images, velocity, and Hα intensity maps from this sample are shown in Fig. 1.

2.1.2 OSIRIS observations (adaptive optics)

We selected the five galaxies above based on the preliminary results of the KGES survey to do follow-up observations with adaptive optics. We prioritized the KGES targets that appeared to have ordered rotation (to more easily measure j_*), as well as proximity to stars that could be used for the tip–tilt correction. We observed four galaxies during 2019 March 13 with the OH-Suppressing Infra-Red Imaging Spectrograph (OSIRIS; Larkin et al. 2006) with the Keck II telescope using laser guide star mode. One of the targets was not useful due to the low signal-to-noise ratio (SNR). The other galaxies (COSMOS 110446, COSMOS 171407 and COSMOS 130477) were observed using the Hn3 filter (*H* band at 15940-16760Å) to cover the redshifted Hα emission line using the 0.1 arcsec plate scale.

For each galaxy, we took eight exposures of 900 s for each target (seven for COSMOS 130477 due to bad weather conditions). The data were reduced using the OSIRIS data reduction pipeline DRP 4.2.0[1] with their appropriate rectification matrices. The OSIRIS PSF FWHM is ~0.1 arcsec for the high SNR data but two galaxies (COSMOS 171407 and COSMOS 130477) had low SNR so we had to apply some spatial smoothing (discussed in Section 3) on the datacubes, leading to the degrading of their spatial resolution as shown in Table 2. The spectral resolution of the datacubes is $R \sim 3800$.
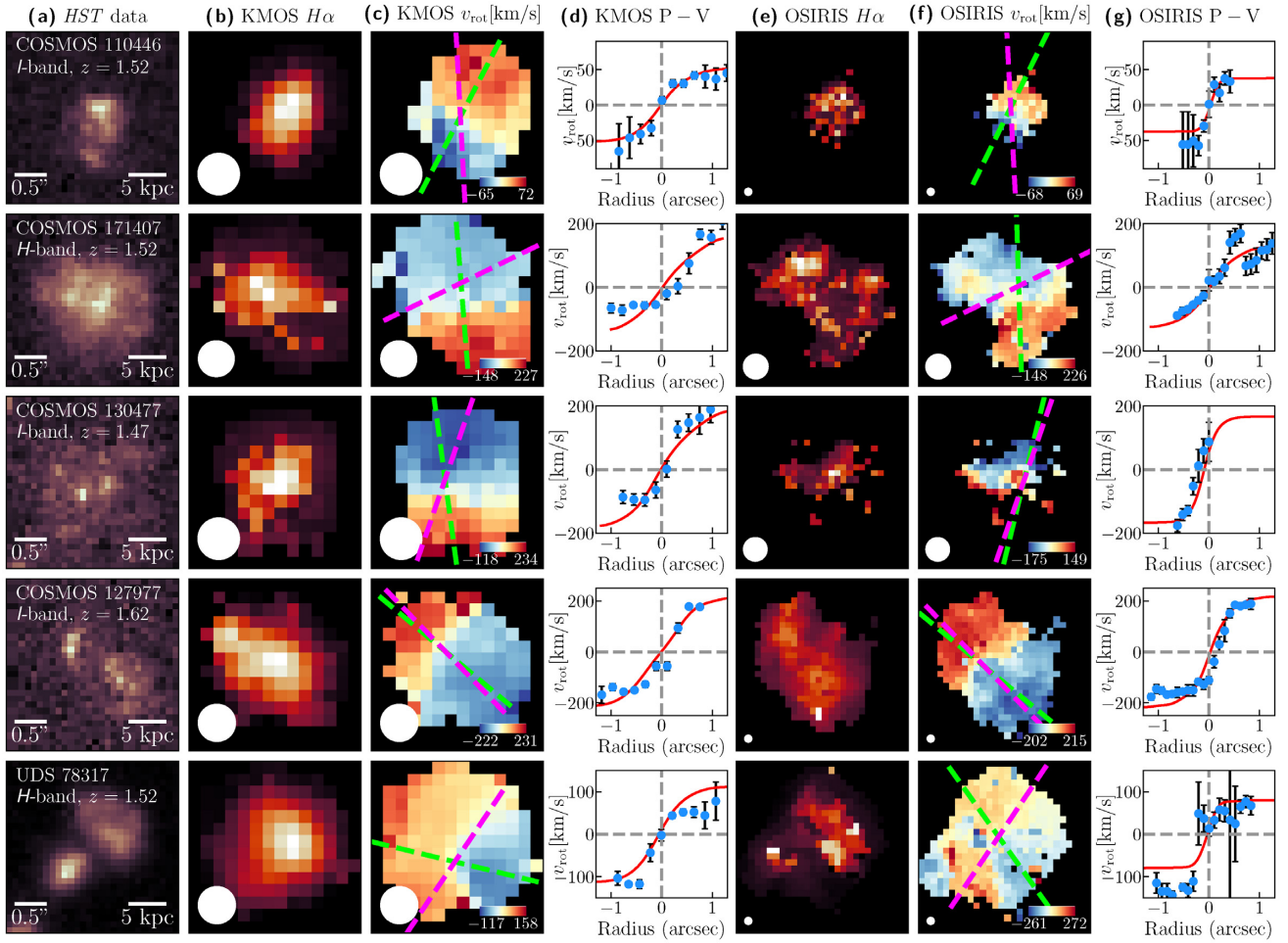
---

[1] https://github.com/Keck-DataReductionPipelines/OsirisDRP

Figure 1. 2D maps of the $z \sim 1.5$ subsample. (a) *HST* broad-band continuum maps with the corresponding redshift and spatial scales. (b) Natural seeing Hα intensity maps from KMOS with the PSF FWHM indicated by the white circle. (c) Extracted velocity fields of the natural seeing data where the green and purple dashed lines indicate the kinematic and morphological main axes, respectively. (d) Position–velocity (P–V) diagrams where blue dots indicate the velocities of the pixels that lay along the kinematic position axis as a function of the projected radius in arcsec. The error bars correspond to the 1σ error from the emission-line Gaussian fit in each spaxel. The red line indicates the velocities along the kinematic position axis of the 2D model built from the individual data. The discrepancies between the model and data points are expected since the points are only along the major axis, whereas the fit is built from the full 2D velocity field. Columns (e), (f), and (g) are the Hα intensity, velocity field, and P–V diagram from the adaptive optics observations from OSIRIS.

Additionally, we included in our sample the two $z \sim 1.5$ galaxies with similar spatial and wavelength resolutions studied in Sweet et al. (2019) (COSMOS 127977 and UDS 78317).

2.2 Sample at $z \sim 2$

Our second set of data was obtained from the public releases of the SINS/zC-SINF (Förster Schreiber et al. 2018) and KMOS^{3D} (Wisnioski et al. 2015) surveys, using the Spectrograph for Integral Field Observations in the Near Infrared (SINFONI; Eisenhauer et al. 2003) and KMOS. The *HST* images, velocity and Hα intensity maps are shown in Fig. 2.

2.2.1 KMOS^{3D} observations (natural seeing)

This seeing limited subsample was selected from KMOS^{3D} which consists of a $0.7 < z < 2.7$ galaxy survey in the near-infrared with K-band magnitudes of $K < 23$, where Hα emission is located in the YJ, H, and K-band filters of KMOS. The five galaxies have a spatial pixel scale of 0.2 arcsec per pixel and the mean PSF FWHM is 0.73 arcsec. The spectral resolution is $R \sim 3975$ at the location of Hα emission.

2.2.2 SINS/zC observations (adaptive optics)

The SINS/zC-SINF AO survey consists of a sample of 35 galaxies in the K band with the SINFONI instrument in adaptive optics mode presented and discussed by Förster Schreiber et al. (2018). This is a follow-up survey to the seeing limited observations of the same galaxies and was designed to resolve the nebular emission and kinematics on scales of $\sim$1.5 kpc. We selected the five galaxies that had available natural seeing limited observations from KMOS^{3D} for our combination method.

The spatial pixel scale of this sample is 0.05 arcsec per pixel and the spectral resolution is $R \sim 4000$ in the K band. The mean PSF FWHM of this sub-sample is 0.17 arcsec.

2.3 HST imaging

We use high-resolution broad-band *HST* imaging of our targets from the Cosmic Evolution Survey (COSMOS; Scoville et al. 2007), UKIDSS UDS (UDS; Lawrence et al. 2007), and Great Observatories Origins Deep Survey (GOODS-South; Giavalisco et al. 2004) extragalactic fields.
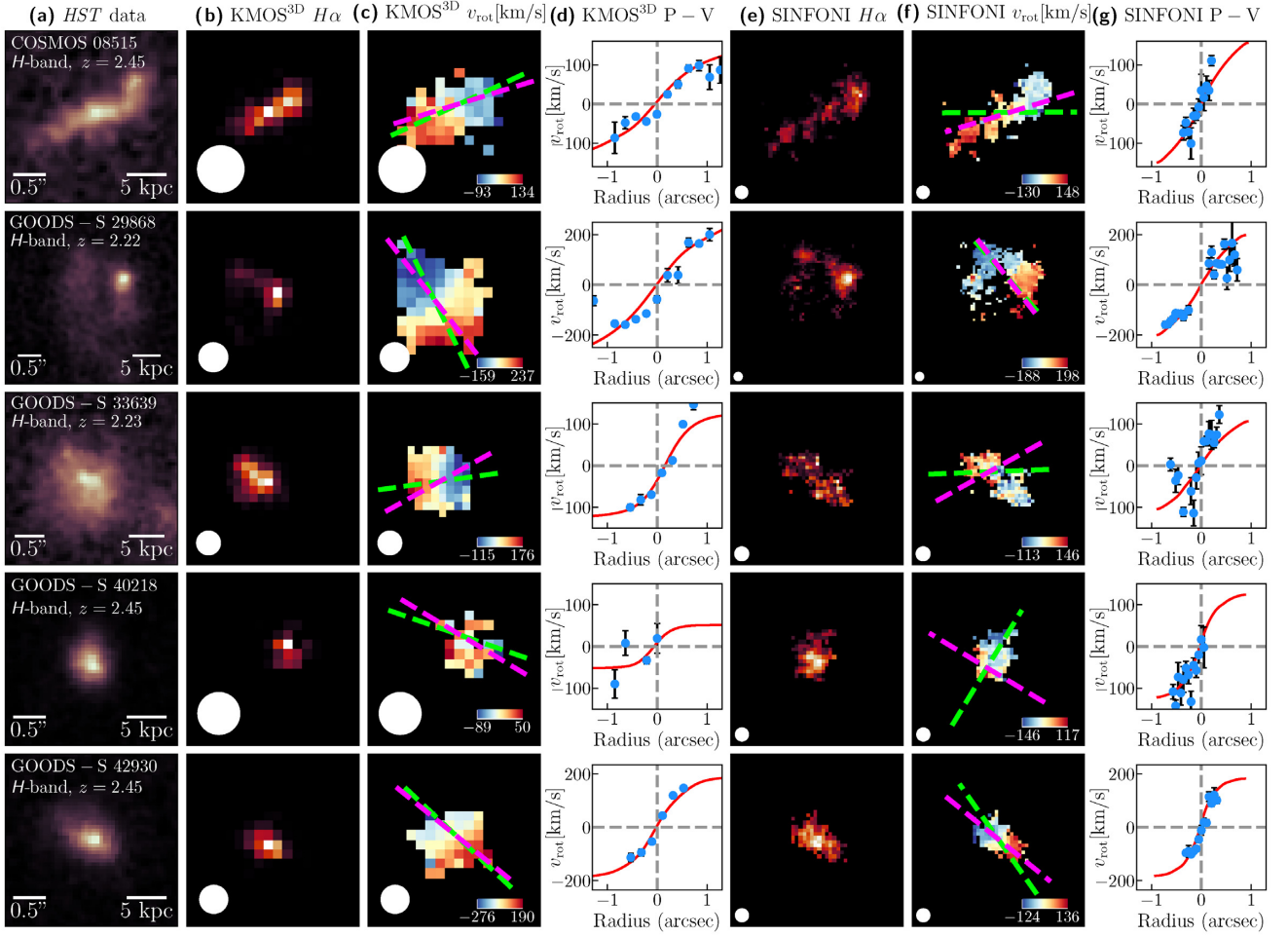
Figure 2. 2D maps of the $z \sim 2$ subsample. (a) *HST* broad-band continuum maps with the corresponding redshift and spatial scales. (b) Natural seeing Hα intensity maps from KMOS^{3D} with the size of the PSF indicated by the white circle. (c) Extracted velocity fields of the natural seeing data where the green and purple dashed lines indicate the kinematic and morphological main axes, respectively. (d) Position–velocity (*P–V*) diagrams, where blue dots indicate the velocities of the pixels that lay along the kinematic position axis as a function of the projected radius in arcsec. The error bars correspond to the 1σ error from the emission line Gaussian fit in each spaxel. The red line indicates the velocities along the kinematic position axis of the 2D model built from the individual data. The discrepancies of the model and data points are expected since the points are only along the major axis whereas the fit is built from the full 2D velocity field. Columns (e), (f), and (g) are the Hα intensity, velocity field, and *P–V* diagram from the adaptive optics sample from SINFONI.

Table 1. Summary of the sample including the galaxy ID, source of the *HST* photometric data, spectrograph used to acquire the data, Right Ascension and Declination in J2000 coordinates, redshift estimated from their Hα emission (from the AO data sets), stellar mass and star formation rate (SFR) measurements from Gillman et al. (2020) ($z \sim 1.5$), and Förster Schreiber et al. (2018) ($z \sim 2$). We adopt typical uncertainties of the stellar properties of 0.2 dex in log (M_*) (Mobasher et al. 2015) and 0.47 dex in log (SFR$_{SED}$).

Galaxy (ID)	*HST* primary data	IFS Instrument (AO + NS)	RA (°)	Dec. (°)	z	M_* (log M$_\odot$)	SFR (M$_\odot$ yr^{-1})
COSMOS 110446	*I*-band (ACS)	OSIRIS + KMOS	149.96164	2.08053	1.5199	10.52	49
COSMOS 171407	*H*-band (DASH)	OSIRIS + KMOS	149.89164	2.34849	1.5247	10.41	31
COSMOS 130477	*I*-band (ACS)	OSIRIS + KMOS	150.00314	2.32999	1.4651	10.41	33
COSMOS 127977	*I*-band (ACS)	OSIRIS + KMOS	149.90790	2.30060	1.6200	10.05	45
UDS 78317	*H*-band (CANDELS)	OSIRIS + KMOS	34.39170	− 5.17110	1.5247	10.49	45
COSMOS 08515 (ZC-410041)	*H*-band (CANDELS)	SINFONI + KMOS	150.18448	2.26626	2.4541	9.88	47
GOODS-S 29868 (K20-ID7)	*H*-band (HLF)	SINFONI + KMOS	53.12133	27.77461	2.2239	10.28	112
GOODS-S 33639 (K20-ID6)	*H*-band (HLF)	SINFONI + KMOS	53.12133	27.75588	2.2348	10.53	45
GOODS-S 40218 (GMASS-2303)	*H*-band (HLF)	SINFONI + KMOS	53.16195	− 27.72266	2.4507	9.85	21
GOODS-S 42930 (GMASS-2363)	*H*-band (HLF)	SINFONI + KMOS	53.16416	− 27.70990	2.4519	10.34	64

Table 2. Resolution parameters of the acquisition stars associated with all the IFS observations. The values marked with ∗ are the galaxies for which we needed to apply spatial smoothing to increase SNR. Strehl in the $z \sim 2$ sample are the quoted values in Förster Schreiber et al. (2018).

	Galaxy	NS FWHM (arcmin)	AO FWHM (arcmin)	Strehl (per cent)
	COSMOS 110446	0.67	0.11	29
	COSMOS 171407∗	0.58	0.39	17
$z \sim 1.5$	COSMOS 130477∗	0.67	0.38	14
	COSMOS 127977	0.60	0.11	29
	UDS 78317	0.60	0.11	29
	COSMOS 08515	0.96	0.16	24
	GOODS-S 29868	0.60	0.15	23
$z \sim 2$	GOODS-S 33639	0.60	0.20	13
	GOODS-S 40218	0.87	0.17	25
	GOODS-S 42930	0.62	0.17	13

For the galaxies in the COSMOS and UDS fields, we use the Cosmic Assembly Near-Infrared Deep Extragalactic Legacy Survey (CANDELS; Koekemoer et al. 2011) in the F160W filter with a pixel scale of 0.06 arcsec per pixel and PSF FWHM of 0.18 arcsec. We also use COSMOS-DASH (COSMOS-Drift And SHift) which is a Wide-Field WFC3 Imaging survey in the COSMOS field (Mowla et al. 2019) with the same filter and pixel scale of 0.1 arcsec per pixel and a PSF FWHM of 0.15 arcsec. For the galaxies in the GOODS-S field, we use the Hubble Legacy Field (HLF; Whitaker et al. 2019) also with the F160W filter and a pixel scale of 0.06 arcsec per pixel and the same PSF size.

The galaxies COSMOS 110446, COSMOS 130477, and COSMOS 127977 do not have available *H*-band images so we use *I*-band[2] *HST* images with the Advanced Camera for Surveys (ACS; Avila 2017) in the F814W filter and a pixel scale of 0.03 arcsec per pixel and PSF FWHM of 0.08 arcsec.

3 METHODS AND ANALYSIS

In this section, we describe the methods used to obtain the photometric and kinematic models and our strategy in dealing with the different resolutions and pixel scales from each data set. We provide the details of the spatial smoothing needed in the two galaxies with low signal-to-noise ratio. We then describe the method used to combine the different resolutions and the capabilities and limitations of our code.

3.1 Hα kinematic maps

We measure the ionized gas kinematics from each galaxy's data cube by fitting a Gaussian profile to the redshifted Hα emission line. From the fit, we extract intensity and velocity maps with their corresponding errors. For the natural seeing data, which has higher SNR, it was possible to include the [NII] doublet in the fitting routine. Given the large contamination from skylines in the near-infrared, the fitting steps must be done carefully and in a consistent manner.

First, we obtain the systemic redshift of each galaxy by fitting a Gaussian profile to the integrated spectrum in the wavelength range where we expect Hα emission (there is good consistency of our measured redshift with respect to the literature values from the KGES and SINS surveys). Then we make a Gaussian fit along the spectral direction in each spaxel to find the redshifted line using MPFIT

(Markwardt 2009) which is a least-squares curve fitting routine. In order to systematically select the real emission only, we use an SNR cut along the spectral axis by comparing the goodness of the Gaussian fit and the goodness of the fit to the continuum, as

$$\mathrm{SNR} = \sqrt{\chi^2_{\mathrm{cont}} - \chi^2_{\mathrm{fit}}}, \tag{1}$$

where χ^2_{cont} is associated with the fit of a straight line to the continuum and χ^2_{fit} is associated with the Gaussian profile fit to the emission line. During the Gaussian fitting, we down-weight the residual skylines in the spectrum to prevent erroneous fits and we only keep the line fits that result in velocities lower than 500 km s^{-1} and a width of at least 1.25 times the width of the skylines, similarly to the procedures employed to the KGES sample in Tiley et al. (2021).

The fitting routine allowed us to obtain the velocity fields for most of our galaxies. However, for the two galaxies from the adaptive optics data set (COSMOS 171407 & COSMOS 130477) with low SNR, we had to smooth the data cubes spatially at the cost of losing spatial resolution and spreading noise through the seeing elements. We applied Gaussian, median filter and Moffat smoothing with different kernel sizes to increase SNR, as shown in Fig. 3. The median filter with a kernel size of 3 pixels provided the largest increase in SNR (a factor of 2) and still preserved a finer resolution than the natural seeing maps so it was our chosen method.

3.2 Spatial resolution

Modelling the point spread functions of each data set is crucial in order to derive intrinsic deconvolved kinematic models. Since the PSF associated with seeing limited observations is significantly different from that with adaptive optics correction, we model them separately throughout this analysis. For the natural seeing data, we fit Gaussian profiles to the acquisition stars during the time of observations (where available) to calculate the PSF size. For the adaptive optics sample, the PSF has a more complex shape with two key components (Davies & Kasper 2012), where the peak component accounts for the adaptive optics correction and the broad component accounts for the uncorrected atmospheric blurring.

The peak component is modelled using an Airy disc profile (Airy 1835) and the broad component using a Moffat profile (Moffat 1969). Additionally, we quantify the efficiency of the adaptive optics correction or Strehl as the ratio of the observed peak intensity in the reference star, compared to the maximum peak intensity of the modelled star at the diffraction limit (i.e. a model star with the same total flux convolved only with the measured Airy disc kernel). Fig. 4 shows the PSF modelling of two of the reference stars from the adaptive optics observations, and Table 2 shows the PSF size of the whole sample.

3.3 Angular momentum

We calculate the stellar specific angular momentum[3] j_* content of the galaxies by assuming cylindrical axisymmetric rotation as in

$$j_* = \frac{\int_0^R 2\pi r^2 \Sigma(r) v(r) \mathrm{d}r}{\int_0^R 2\pi r \Sigma(r) \mathrm{d}r}, \tag{2}$$

where $\Sigma(r)$ and $v(r)$ are the one-dimensional models of the surface mass density and velocity field profiles respectively. In order to

---

[2]*I*-band is a bluer band so these images provide a less accurate representation of the stellar mass distribution.

[3]Using j_* instead of J_* is a common practice in kinematic studies because it removes the stellar mass scaling $\left(j_* = \left| \frac{J_*}{M_*} \right| \right)$, while combining the disc size and rotation velocity profile.
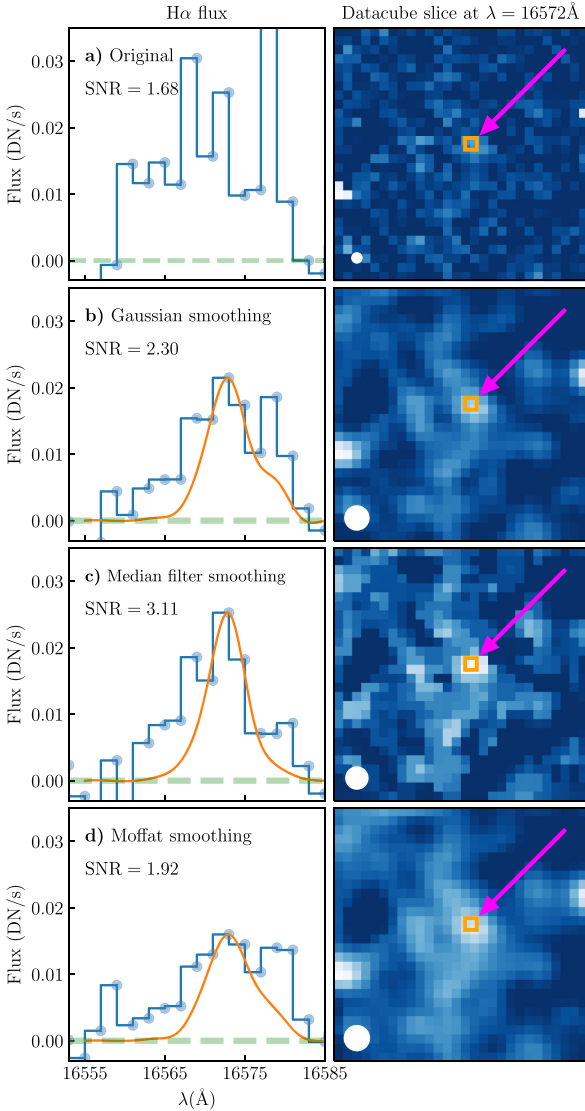
Figure 3. Left-hand panels: (a) Spectrum covering Hα emission along the direction of a single spaxel (indicated by the orange square in the right panels) from the original data cube of COSMOS 171407. Panels (b), (c), and (d) are the spectra after applying Gaussian ($\sigma = 1$ pix), median filter (size = 3 pix), and Moffat smoothing (core size = 2 pix), respectively. The green dashed line represents the continuum level. We opt for method (c) that results in a significant improvement in the signal-to-noise ratio. Right-hand panels: The slice of the datacubes at $\lambda = 16572$Å to visualize the effect of the smoothing where the size of the PSF is shown at the bottom left corner. The pink arrow indicates the location of the spectrum shown in the left-hand panel.

infer the resolved stellar mass profiles, we adopt the model of an exponential disc:

$$\Sigma(r) = s_d \exp\left(\frac{-r}{r_d}\right), \tag{3}$$

where r_d is the characteristic disc scale length and s_d is the surface mass density normalization factor. The surface density model is obtained using a maximum likelihood estimation using the *HST* photometric maps with r_d, position angle, inclination and centre coordinates as free parameters and convolving the model with the *HST* PSF in each case. For the initial guess of the disc size r_d we use the reported values of r_{eff} from Gillman et al. (2020) and

Förster Schreiber et al. (2018) (where $r_{eff} = 1.68 r_d$ for an exponential disc)[4], while for the deprojection parameters we use the best-fitting parameters from an initial iteration of the kinematic fit. Besides defining the extent of the stellar mass density model, the measured scale length allows us to quantify the radii where the bulk of angular momentum resides in terms of a characteristic size.

There are various systematics associated with the chosen surface density modelling. First, the morphological complexity of each individual system is not accounted for, as the model does not include additional components such as a thick disc, a central bulge or bright massive clumps. The assumed exponential profile is a simplification that aids consistency in the method and facilitates a reference scale but can potentially lead to over- (or under-) estimations of the stellar mass content.[5] Secondly, the analysis of the light distribution is limited to their *H*-band (or *I*-band) imaging which is not representative of all the stellar populations within the galaxies. This can lead to a systematic bias in the total stellar mass distribution and can affect the determination of the photometric centre measurement since the brightest region does not necessarily coincide with the kinematic centre of the galaxy.

Lastly, since we are interested in the *specific* angular momentum, we do not need to explicitly assume a mass-to-light ratio $(M/L)_*$, as it appears on both the numerator and denominator of equation (2), however this assumption implies that the surface mass density profile is dependent only on one stellar population with no additional components. If the galaxies do have other components such as central bulges with a larger concentration of old stellar populations, then the galaxy mass-to-light ratio is not expected to be constant. We quantify these effects in Section 4.7, where we use complementary *J*- and *H*-band imaging (available for the $z \sim 2$ sample from Tacchella et al. (2015) via private communication) to estimate the $(M/L)_*$ ratio differences in the *J*–*H* colour profiles and the effect of a central bulge and clump components in the measurement of j_*.

The chosen functional form of the rotation curve $v(r)$ is one characterized by an asymptotic velocity v_{flat} and the distance r_{flat} proposed by Boissier et al. (2003). This choice is based on the overwhelming evidence that rotation curves flatten at large radii for low and high-redshift disk galaxies (van de Hulst, Raimond & van Woerden 1957; Carignan et al. 2006; Catinella, Giovanelli & Haynes 2006; de Blok et al. 2008; Zasov et al. 2017; Tiley et al. 2019b; Marasco et al. 2019) and is given by

$$v(r) = v_{flat}\left(1 - \exp\left(\frac{-r}{r_{flat}}\right)\right). \tag{4}$$

The velocity profile $v(r)$ is obtained from the IFS data based on the assumption that the kinematics of the ionized gas is an acceptable tracer of the motions of the stars. At $z \sim 0.1$, a direct comparative study of two star-forming galaxies considered to be analogues of high redshift clumpy discs from the DYNAMO survey (Bassett et al. 2014) found that the stellar kinematics are closely coupled to the kinematics of the ionized gas. Similarly, Guérou et al. (2017) found a similar conclusion for a sample of 17 galaxies at intermediate redshift ($0.2 \leq z \leq 0.8$). However, this remains untested directly at $z > 1$ given the observational challenges in measuring stellar

---

[4]Note that the r_{eff} values from Gillman et al. (2020) were obtained from a more general Sérsic's profile fitting with GALFIT, where n is in the range of [0.2,8] and thus they naturally differ from our measurement.

[5]The radial surface brightness profiles $\Sigma(r)$ of 6/10 galaxies in this paper follow an exponential decay to within 10 per cent. The rest of the sample (4/10) are within ∼26 per cent with GOODS-S 29868 having the largest rms residual errors (∼25.7 per cent) due to its complex light distribution.
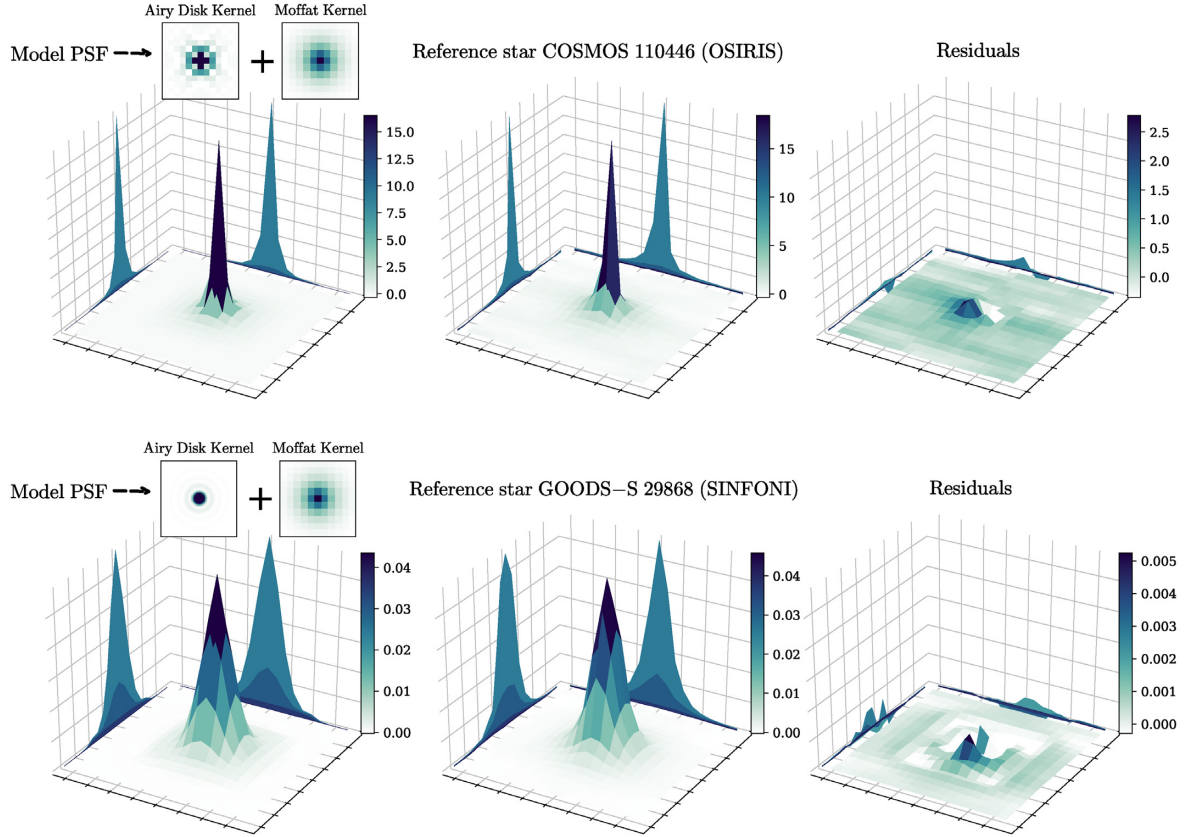
Figure 4. 3D visualization of the PSF modelling on the acquisition stars of COSMOS 110446 (top) and GOODS-S 29868 (bottom) with the peak (Airy disc) and broad (Moffat) components. Left-hand panels show the modelled PSF as well as the 2D visualization of the two components, middle panels show the flux from the reference stars, and right-hand panels show the residuals. The pixel scale of the instruments used in these observations (OSIRIS and SINFONI) are different as shown by the background projections of the data and models.

kinematics directly (Bezanson et al. 2018) and only feasible when facilities such as JWST come online. Thus, using $v(\mathrm{H}\alpha)$ as a proxy for v_* has been a common approach in multiple $z > 1$ IFS studies (e.g. Burkert et al. 2016; Swinbank et al. 2017) that assume a small effect of the increased star formation activity at $1 < z < 3$.[6] In this work, we follow the same assumption but note that it can lead to systematic uncertainties at the ~ 0.1 dex level as estimated with the SAMI survey at $z = 0$ by Cortese et al. (2016).

To measure the kinematics, we use a maximum likelihood estimation where the free parameters are r_{flat} and v_{flat} as well as the position angle θ_{PA}[7] and kinematic centre coordinates $[x_0, y_0]$. The inclination i is constrained from a fit to the surface brightness profile to break the degeneracy with the velocity field as explained in more detail in Section 4.4.

A two-dimensional kinematic modelling approach, where 2D velocity field models are smoothed by the PSF to resemble the extracted velocity fields (e.g. GIPSY, van der Hulst et al. 1992; RINGFIT, Simon et al. 2003; NEMO, Teuben 2004; KINEMETRY, Krajnović et al. 2006; DISKFIT, Sellwood & Spekkens 2015) is only accurate if the pixel-to-pixel variations in surface brightness are

negligible, which is not the case for the sample in this work. A full 3D approach, where intensity cubes are smoothed to resemble the real data cubes is computationally expensive and is limited to single resolution measurements in the publicly available codes (e.g. TIRIFIC, Józsa et al. 2007; DYSMAL, Cresci et al. 2009; GALPAK³ᴰ, Bouché et al. 2015; GalPaK³ᴰ, Bouché et al. 2015; ³ᴰBAROLO, di Teodoro & Fraternali 2015; GBKFIT, Bekiaris et al. 2016).

For these reasons, and in order to make a kinematic modelling that accounts for the difference in the emission line intensities, we use what we call a hybrid '21/2D' approach. It consists of creating model cubes using the galaxy size and kinematic parameters with an intensity profile based on the *HST* imaging. We then convolve the cubes using the modelled PSF and extract the velocity fields to find those that best resemble the real $v(x, y)$ data. The accuracy of the modelling is quantified using simulations and it is explained in detail in Appendix A. An example of the velocity field model and its residuals for one of the galaxies in our sample is shown in Fig. 5.

We define j_* as the *total* stellar specific angular momentum, which represents the asymptotic value at $r \to \infty$ from equation (2). We find that in our sample, j_* approaches the asymptotic value (at least at a >95 per cent level) at $4r_{\mathrm{eff}}$ as discussed in more detail in Section 4.5, so we take the total stellar specific angular momentum j_* at the arbitrary value of $r = 10r_{\mathrm{eff}}$ that ensures convergence. Additionally, we compute the commonly used approximation of j_* for high-redshift galaxies from Romanowsky & Fall (2012) as

$$\tilde{j}_* \approx k_n v_s r_{\mathrm{eff}}, \tag{5}$$

[6] The increased supernovae feedback in star-forming galaxies drives outflows and winds that can affect the gas kinematics throughout the disc.
[7] A visual inspection of the *HST* maps shows that the θ_{PA} measured from kinematics is more reliable than that of photometry, especially since it is constrained with two different data sets.
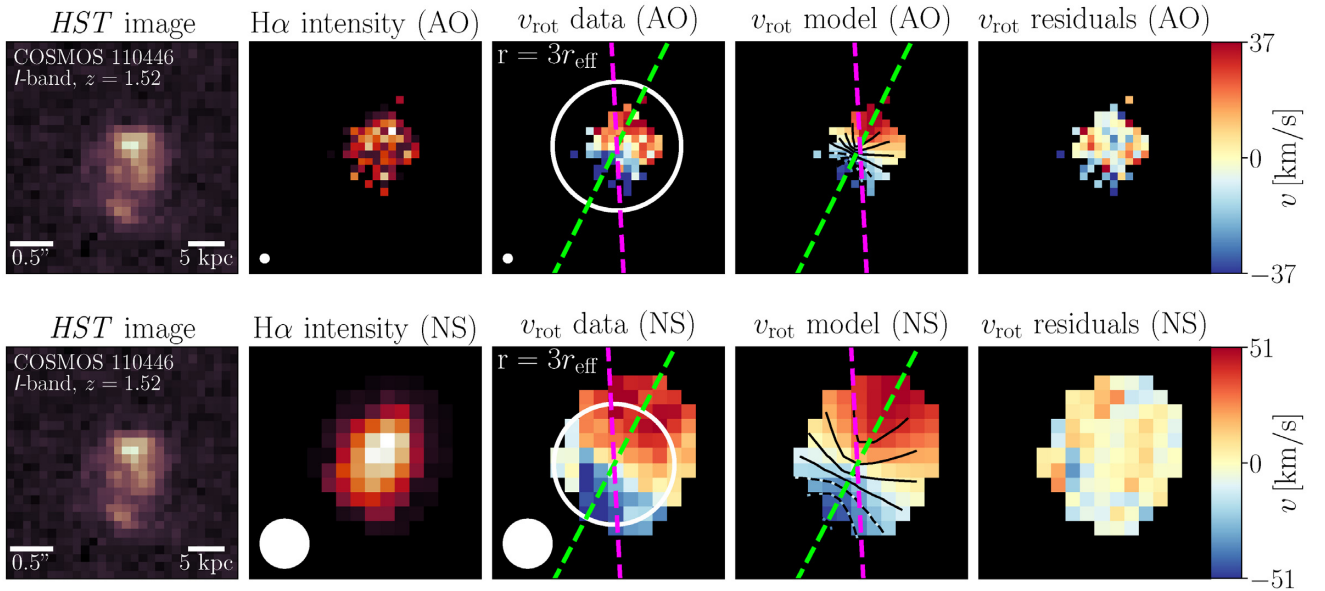
Figure 5. Example of the kinematic fit of galaxy COSMOS 110446 at the individual resolutions (top row for AO and bottom row for NS). From left to right: *HST* image, Hα intensity map, velocity field, best model from the fitting routine and residuals. The purple and green dashed lines represent the morphological and kinematic main axes, respectively. The colour bar is the same for all of the kinematic maps. The frames are not aligned to the continuum centre but this is accounted for in the modelling.

where the factor v_s is the characteristic rotation velocity evaluated at $2r_{eff}$ and k_n is a spatial weighting factor which is a function of the Sérsic index $k(n)$ with $k_n = 1.19$ for an exponential profile.

We compute angular momentum from each data set separately, but we also perform a combined measurement to improve the kinematic modelling and explore the capabilities and restrictions of the individual measurements. This combination method is explained in detail in the next section.

3.4 The combination method

To combine both natural seeing and adaptive optics observations of a single galaxy, we have developed a maximum likelihood estimation kinematic fitting code (see Appendix A). The method combines:

(i) Adaptive optics enabled high-resolution data (from Keck/OSIRIS and VLT/SINFONI) for the steep rising part of the rotation curve where the SNR is enough to prevail over the loss in throughput introduced by the adaptive optics correction and

(ii) Natural seeing low-resolution data (from VLT/KMOS) to measure the flat part of the rotation curve where the bulk of angular momentum resides. At these radii, the effects of beam smearing are smaller and the SNR tends to be higher than at corresponding distances in adaptive optics assisted observations.

The algorithm, as illustrated in Fig. 6 works as follows: A model cube with the varying input parameters is created, the cube is degraded with the PSF and pixel scale of the natural seeing and adaptive optics data respectively using the corresponding convolution (single Gaussian kernel for natural seeing and Airy disc + Moffat kernel for adaptive optics), the velocity fields are extracted from the convolved cubes and the best model is the one that yields the maximum likelihood from the two data sets. The photometric maps are fitted separately in each case with a similar maximum likelihood approach.

There are multiple advantages to this method. First, it makes use of the kinematic information of the same galaxy obtained with two

instruments with different sensitivities, spatial resolutions and pixel scales. Second, the convolution with the respective PSF is done separately (but simultaneously), which helps mitigate the effects of systematic errors from single modelling. Lastly, this method gives the code the freedom to centre the two models at separate spatial locations so the possible differences in the alignment of the images (of a few pixels) are accounted for. We analyse the usefulness of this combination model-fitting method by comparing it to the single model fitting as discussed in Section 4.

4 RESULTS AND DISCUSSIONS

The high-redshift sample studied in this paper is to date the largest sample with angular momentum measurements from the combination of high- and low-spatial resolution data. Consequently, we can address the relevance of a combination method. Throughout this section, we discuss the effect of combining the different resolutions in the determination of rotation velocity profiles, kinematic state as well as the convergence of $j_*(r)$ to the asymptotic value j_*. Table 3 shows the main results of the modelling and additional figures are included in the supplementary (online) section.

4.1 Classification as rotating discs

High-spatial resolution observations, to sub-kpc scales, are necessary to accurately determine the kinematic state of a galaxy and resolve large star-forming clumps (Law et al. 2007; Genzel et al. 2008; Epinat et al. 2012; Livermore et al. 2015; Mieda 2015; Wisnioski et al. 2015; Fisher et al. 2017; Förster Schreiber et al. 2018; Sweet et al. 2019). In our full sample, the mean PSF FWHM of the adaptive optics sample (∼0.15 arcsec) corresponds to ∼1.3 kpc, whereas the seeing-limited sample (∼0.69 arcsec) corresponds to ∼5.7 kpc. In the high-resolution data, additional components with proper line-of-sight velocities become visible as indicated in Fig. 7.
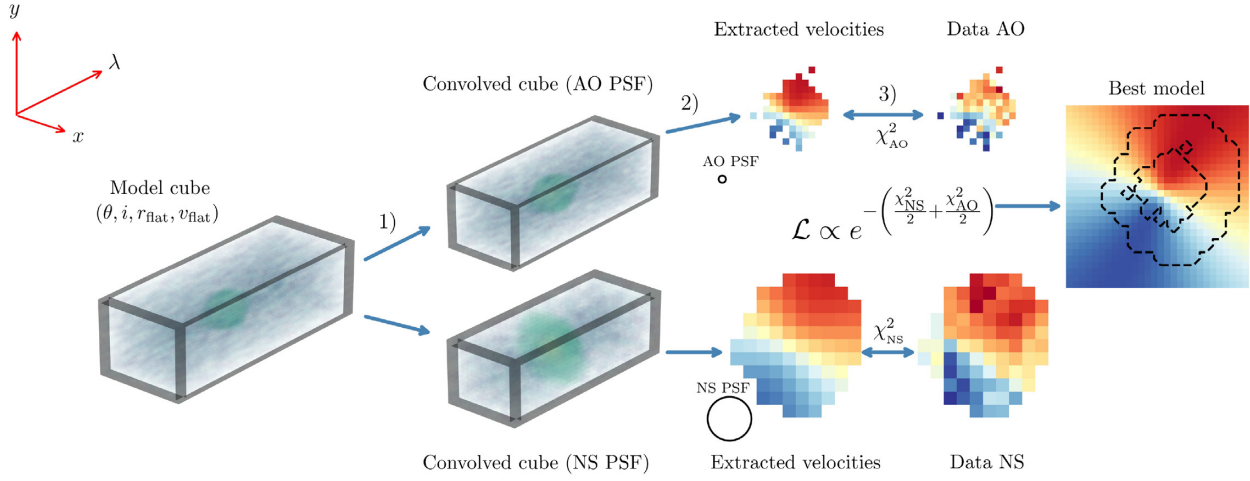
Figure 6. Representation of the kinematic modelling of our combination method. In step (1) the model cube is convolved using the different data PSF separately. Step (2) is the extraction of the velocity fields from the convolved model cubes. Step (3) is the likelihood estimation based on the combination of the two χ^2 values (χ^2_{NS} and χ^2_{AO}), where the best kinematic model is obtained by maximizing that likelihood.

Table 3. Measured parameters of our kinematic and photometric modelling. Galaxies in italics are classified as mergers (see Section 4.1) so their fit values are used for reference and comparison with the rest of the sample. From left to right: Galaxy ID, type of IFS data (or instrument), position angle θ_{PA}, inclination i, disc scale length r_d, characteristic radius of the rotation profile r_{flat}, asymptotic velocity v_{flat}, velocity dispersion σ, total angular momentum j_*, and the approximation $\tilde{j}_*$ defined in equation (5). The uncertainties of the kinematic parameters as well as in j_* are explained in Section 4.3.

| Galaxy ID	Data Type	θ_{PA} (°)	i (°)	r_d (kpc)	r_{flat} (kpc)	v_{flat} (km/s)	σ (km/s)	j_* (kpc km s^{-1})	$\tilde{j}_*$ (kpc km s^{-1})
	KMOS	62.5 ± 4.3	51 ± 7.1	1.4 ± 0.3	2.35 ± 1	67.5 ± 11.4	37.5 ± 6.4	142.5 ± 99.2	164
COSMOS 110446	OSIRIS	63.8 ± 7.9	51.3 ± 8.8	1.4 ± 0.2	0.51 ± 1	48.6 ± 19.5	22.1 ± 5.7	133.5 ± 62.5	136
	Combined	63.3 ± 2.4	49.2 ± 6.4	1.4 ± 0.1	2.02 ± 0.8	69.3 ± 7.9		154.1 ± 56.4	175.6
	KMOS	274.5 ± 8.3	48.2 ± 17.3	2.4 ± 0.2	8.84 ± 1.5	306.9 ± 35	97.6 ± 27.3	756.5 ± 251.6	887.6
COSMOS 171407	OSIRIS	271.8 ± 4.1	46.1 ± 14.6	2.4 ± 0.2	3.31 ± 1.1	185.6 ± 23.2	81.8 ± 36.8	717.3 ± 158.5	814.9
	Combined	274.8 ± 1.3	50.8 ± 7.1	2.4 ± 0.1	5.91 ± 0.5	226.4 ± 7.2		695.8 ± 112.6	813.3
	KMOS	277.7 ± 5	37.5 ± 11.4	2.4 ± 0.2	5.59 ± 1.4	354.1 ± 19.8	89 ± 14.3	1117.6 ± 369	1304.8
COSMOS 130477	OSIRIS	256.3 ± 13.8	39.1 ± 14.1	2.4 ± 0.2	1.35 ± 1.4	265 ± 52.3	56.3 ± 10	1212.7 ± 281.7	1268.5
	Combined	269.2 ± 1.5	35.8 ± 8.4	2.4 ± 0.1	2.07 ± 1.1	267.7 ± 7.3		1157.4 ± 220.8	1259.5
	KMOS	140.2 ± 8.2	65.2 ± 18.1	2.1 ± 0.2	3.41 ± 1.4	250.9 ± 28.1	103.7 ± 20.3	804 ± 294.5	923.3
COSMOS 127977	OSIRIS	140.6 ± 2.3	65.1 ± 5.3	2.1 ± 0.2	2.27 ± 0.5	243.5 ± 14.3	82 ± 25.1	879.4 ± 167.3	978.3
	Combined	137.6 ± 1.2	65.1 ± 4.4	2.1 ± 0.1	3.13 ± 0.4	252.4 ± 7.4		832.8 ± 132.3	951.5
	KMOS	166.4 ± 9.7	33 ± 13.2	1.7 ± 0.2	2.33 ± 1.8	209.6 ± 28	97.5 ± 22.4	574.9 ± 200.8	652.6
UDS 78317	OSIRIS	125.5 ± 9.7	36.9 ± 17.4	1.7 ± 0.2	0.62 ± 1.6	133 ± 38.7	105.3 ± 31	443.6 ± 161.8	452
	Combined	143.3 ± 1.4	37.2 ± 5.1	1.7 ± 0.1	1.12 ± 0.6	128.8 ± 8.5		410.5 ± 112.1	435.2
	KMOS	204.9 ± 8.5	81.7 ± 4	2.9 ± 0.2	6.37 ± 1.1	154.1 ± 20.2	75.9 ± 8.5	603.8 ± 360.7	703.2
COSMOS 08515	SINFONI	180.4 ± 5.7	81.7 ± 7.7	2.9 ± 0.2	6.92 ± 1.1	245.2 ± 23.5	81.7 ± 13.8	924.5 ± 197.8	1072.7
	Combined	189.3 ± 3.7	81.6 ± 2.3	2.9 ± 0.1	6.98 ± 0.4	262.9 ± 7.8		987.2 ± 95.9	1145.6
	KMOS	296 ± 15	64.6 ± 35.9	2.8 ± 0.2	8.2 ± 1.2	361.3 ± 31.4	88.3 ± 17	1185.1 ± 529.6	1389.3
GOODS-S 29868	SINFONI	311.7 ± 2.9	62.1 ± 11	2.8 ± 0.2	6.83 ± 0.8	346.8 ± 23.6	101.2 ± 28.5	1249.2 ± 205.4	1459.5
	Combined	302.2 ± 1.8	62.1 ± 5.9	2.8 ± 0.1	6.89 ± 0.4	343.9 ± 11.5		1233.5 ± 103.7	1441.5
	KMOS	187.9 ± 22.9	32.1 ± 9.9	3 ± 0.2	2.39 ± 2.1	230 ± 33	78 ± 10.8	1259.7 ± 688.8	1360.2
GOODS-S 33639	SINFONI	182.3 ± 18.8	33.1 ± 22	3 ± 0.2	6.51 ± 2.4	287.3 ± 32.7	89.8 ± 19.6	1170.8 ± 412.7	1205.5
	Combined	187.9 ± 4.3	34.3 ± 6	3 ± 0.1	6.11 ± 1.1	297.8 ± 12.1		1247.7 ± 143.8	1290.1
	KMOS	160.9 ± 16.8	52.4 ± 16.6	1.1 ± 0.2	0.51 ± 1.6	66.3 ± 30.4	109.7 ± 40.2	141.2 ± 153.7	145.7
GOODS-S 40218	SINFONI	238.8 ± 17.1	52 ± 18.1	1.1 ± 0.2	2.52 ± 1.3	166.1 ± 40.6	123.3 ± 29	242.1 ± 103.6	282.5
	Combined	232.4 ± 6.4	49 ± 11.6	1.1 ± 0.1	1.45 ± 0.7	112.1 ± 10.6		201.3 ± 44.1	227.8
	KMOS	316.8 ± 16	58.8 ± 28.3	1.6 ± 0.2	2.97 ± 1.7	229.4 ± 29.7	70.1 ± 11.2	532.6 ± 321.8	616.5
GOODS-S 42930	SINFONI	305.1 ± 5.9	58.8 ± 11.4	1.6 ± 0.2	1.93 ± 0.5	219.4 ± 24.1	64.5 ± 11.6	587.3 ± 162.5	659.9
	Combined	311.4 ± 2.8	57.7 ± 16.6	1.6 ± 0.2	2.38 ± 0.5	229.4 ± 11.3		577.1 ± 62.2	659.1
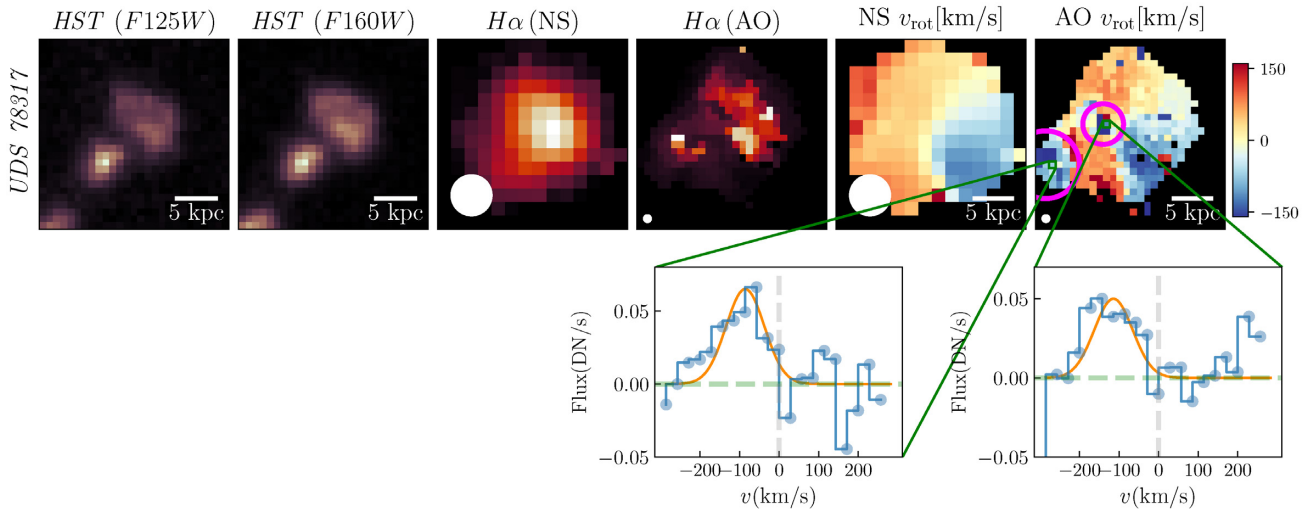
Figure 7. Various maps of galaxy *UDS 78317* that appears to be a rotating disc from natural seeing kinematics but shows a complex kinematic state at high-resolution as well as from photometry. From left to right: *J*- and *H*-band *HST* imaging, Hα intensity maps at low and high resolution and velocity fields at the two resolutions sharing the same colour bar. Purple circles in the adaptive optics map indicate the kinematic components that are absent in the natural seeing counterpart, with the bottom panels showing the detected Hα emission as a function of radial velocity in the zoomed-in pixels. The maps have different pixel scales as well as different PSF sizes as shown by the white circles at the bottom left of each panel.
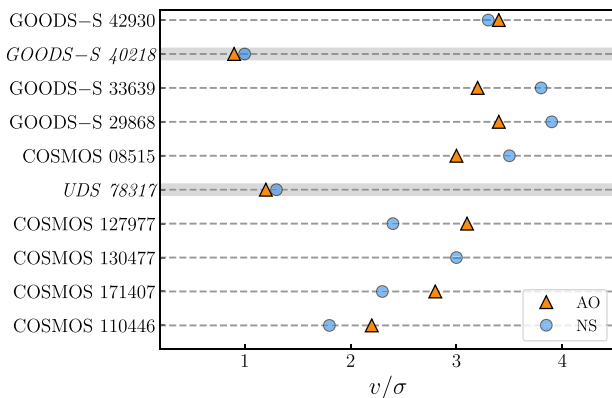
Figure 8. v/σ ratios for the ten galaxies from the NS and AO data sets used for the disc/merger classification. Blue points indicate the measurements from low resolution, and orange triangles indicate the measurements from the adaptive optics data. Grey horizontal lines indicate the mergers *UDS 78317* and *GOODS-S 40218*, which have the lowest values in v/σ (<1.5) at both resolutions.

Another way to assess the kinematic state of the sample is by determining the dynamical support using the v/σ ratio. Following Genzel et al. (2006), a system is considered dispersion supported for $v/\sigma < 1$, and rotation supported for $v/\sigma > 1$. However, as discussed by Tiley et al. (2019a), a galaxy is truly supported by its rotation when $v/\sigma > 3$. In our sample, we use $v_{\rm flat}$ for the velocity v and for the velocity dispersion σ we take the median of the annulus at $r = 1.5r_{\rm eff}$ in the moment two maps, where the effects of beam smearing are lower. The v/σ ratios at both resolutions are shown in Fig. 8.

A commonly used approach to classify high-redshift galaxies as discs from their 2D kinematic maps (e.g Förster Schreiber et al. 2018; Wisnioski et al. 2019) consists of a set of criteria based on their rotation and dispersion profiles. These criteria (as proposed by Wisnioski et al. 2015) are as follows:

(i) A smooth monotonic velocity gradient across the galaxy, defining the kinematic axis
A centrally peaked velocity dispersion distribution with maximum at the position of steepest velocity gradient, defining the kinematic centre
(ii) Dominant rotational support, quantified by the v/σ ratio
(iii) Co-aligned morphological and kinematic major axes (aka kinematic misalignment)
(iv) Spatial coincidence of the kinematic and morphological centres.

We follow these criteria, the results from running the kinematic code and the visual inspection of the photometric maps to classify our sample: Galaxy UDS 78317 has four kinematic poles in the high-resolution map, the morphological and kinematic centres do not align, there is a large misalignment of the kinematic and morphological positions angles and it has a bright companion as seen in the *HST* images (see Fig. 7), thus we classify it as a major merger in agreement with Sweet et al. (2019). GOODS-S 40218 is very compact and only a few pixels surpass the SNR threshold in the Gaussian fit at the two resolutions. Given these limitations, and based on the disordered velocities from both datasets and low v/σ ratios (1 for NS and 0.9 for AO), we classify this galaxy as a merger noting the large uncertainties. For the remainder of the analysis, we label these two galaxies in italics (*UDS 78317* and *GOODS-S 40218*) throughout the paper to distinguish them from the rotating discs.

We treat COSMOS 171407 as a disc due to its ordered rotation but we note its complex structure in the AO Hα intensity map and a kinematic anomaly that is completely absent in its natural seeing counterpart, which is consistent with a minor merger. Galaxy GOODS-S 33639 has only a few pixels with enough SNR for the Hα Gaussian fit as well as poorly constrained inclinations from photometry and kinematics. However, it fulfils the conditions to be classified as a disc. The rest of the galaxies (COSMOS 110446, COSMOS 130477, COSMOS 127977, COSMOS 08515, GOODS-S 29868, and GOODS-S 42930) are classified as discs. In summary, 2/10 galaxies in our sample are classified as mergers (*UDS 78317* and *GOODS-S 40218*), 8/10 are classified as discs with two of them

(COSMOS 171407 and GOODS-S 33639) being largely uncertain. We discuss each individual case in further detail in the supplementary (online) section.

From similar disc/merger classifications, recent kinematic surveys have measured the fraction of discs (f_{disc}) at cosmic noon and at later times. At an intermediate redshift range of $0.9 \leq z \leq 1.6$, Epinat et al. (2012) found $f_{disc} \sim 44$ per cent with the MASSIV survey for 50 star-forming galaxies, most of which were observed at low spatial resolution. Some larger (seeing-limited only) surveys at $z > 1$ have found disc fractions as large as 70–80 per cent (e.g Wisnioski et al. 2015, 2019; Stott et al. 2016). However, that range decreases to $f_{disc} = 50$–60 per cent for the 35 galaxies assisted by adaptive optics studied in Förster Schreiber et al. (2018). Our results are consistent with those of the $z > 1$ seeing limited surveys. However, it is worth noting that the five galaxies chosen from the KGES sub-sample ($z \sim 1.5$) were galaxies that at low resolution appeared to be rotating, had flat rotation curves and well-behaved dispersion profiles. This introduces a selection bias, so the 1:5 ratio of galaxies misclassified as discs is a lower bound on this systematic uncertainty. For larger samples, with a wider range in parameter space, this ratio is likely to be higher.

4.2 Angular momentum measurements

We can use our angular momentum measurements to assess their consistency with known relations. One of these relations is the scaling of stellar specific angular momentum and stellar mass typically known as the 'Fall relation' (Fall 1983). The power law that relates these quantities is well established at $z \sim 0$ in the form $j_* \propto M_*^\beta$ with $\beta \sim 0.58$ for discs and $\beta \sim 0.83$ for bulges (Fall & Romanowsky 2018).

In Fig. 9, we plot the eight discs in the j_* versus M_* map as well as the results from other studies that make predictions on the Fall relation at various redshift ranges (Fall & Romanowsky 2013; Swinbank et al. 2017; Posti et al. 2018; Gillman et al. 2020; Bouché et al. 2021). Since j_* is measured more precisely using both resolutions (as shown in Appendix A), we use those values to find the scaling law that best describes the eight disc galaxies (we exclude the mergers *UDS 78317* and *GOODS-S 40218*). We use the relation $\log(j_*) = \alpha + \beta(\log(M_*/M_\odot) - 10.1)$, where β is the slope from the commonly used $j_* \propto M_*^\beta$ relation and α is the normalization. In Table 4, we show the best-fitting parameters to the unconstrained model (free α and β) as well as a model with a fixed power-law slope $\beta = 2/3 = 0.66$.

From our small sample, we find a scatter of 0.38 dex, which occupies a similar parameter space in the j_* versus M_* relation as the majority of the measurements from Gillman et al. (2020) where they used 201 spatially resolved (seeing limited) galaxies at $z \sim 1.5$ with a scatter of 0.56 dex. The constrained fit ($\beta = 2/3 = 0.66$) to their sample has a small positive offset in the vertical axis ($\Delta\alpha = 0.08 \pm 0.11$) as compared to our constrained fit.

The small difference could be explained by the different mass distribution estimates from their photometric models that are more general (Sérsic models with $n = 0.2-8$) than our assumed exponential discs ($n = 1$). There are also systematic differences associated with the chosen velocity profile, which in their case is measured at the kinematic position angle instead of the full velocity field. In their measurement, there could be objects that show ordered rotation at low resolution but that could be mergers when seen with high spatial resolution. We note that the limited number of objects in our sample and the small mass range provide little diagnostic ability on the slope of the j_* versus M_* relation.

According to the Fall relation, low-M_* ($\leq 10^{10} M_\odot$) galaxies have a low j_* content so they are more susceptible to fragmentation due to a higher prevalence of galaxy-wide instabilities. Thus, they are better candidates for addressing the effect of angular momentum in driving clumpiness and are critical for constraining the low-j_* regime in the j_* versus M_* relation. Constraints in the low-mass regime ($8 \leq \log(M_*/M_\odot) \leq 10.5$) of the Fall relation have been found at an intermediate redshift range ($0.2 \leq z \leq 1.4$) by Contini et al. (2016) and Bouché et al. (2021), using seeing-limited observations with the Multi Unit Spectroscopic Explorer (MUSE; Bacon et al. 2010). In our sample, the only galaxy with trustworthy results in the low-M_* regime is COSMOS 08515. Part of the reason is that the $z \sim 1.5$ sample is biased towards high-j_*, as the targets chosen to be observed with adaptive optics with OSIRIS were the ones that appeared to be large disks with ordered rotation from the natural seeing observations in the KGES survey. A combined (NS + AO) analysis of galaxies in the low-mass regime is thus necessary to impose better constraints on the j_* versus M_* relation at the redshift of interest.

Another important measurement is the contribution of each data type in the total measurement of j_* in terms of their spatial extent. In the combined analysis, we measure the contribution of the individual data sets by measuring the amount of angular momentum in the model enclosed within the boundaries of the high- and low-resolution maps, respectively, as shown in Fig. 10. The adaptive optics data, with its sensitivity limitations, contributes to a mean value of $\sim$72 per cent of total j_* whereas the natural seeing maps reach $\sim$86 per cent. The combination is thus ideal since the adaptive optics data aids a more precise measurement of the rotation profile in the inner radius, and natural seeing aids the measurement of the bulk of j_* which is built at large radii, where the rotation curve is expected to flatten and the effects of beam smearing are smaller.

4.3 Uncertainties in the angular momentum measurements

In order to quantify the uncertainties in the measurement of j_* associated with the individual and combined fits, we resample each galaxy 100 times and run the same analysis for each iteration. To do this, we create a perfect model cube from the best-fitting parameters using the pixel scale of the data and masking out empty pixels. We then convolve with the PSF and extract the velocity field from the convolved cube. Next, in order to recreate the observational errors, we take the residual velocity field (the difference between the best kinematic model and the real velocity field) and resample it with a normal distribution in each pixel. This new error map is then added to the model velocity field. This empirical approach better captures the contribution of artifacts and substructure that are not covered by the kinematic model, since they manifest in the residual velocity fields. If we used the Gaussian line fit errors instead, we would get unrealistically low uncertainties since the residuals are typically 0–70 km s^{-1} compared to the formal errors of $\sim$15 km s^{-1} from the Gaussian line fits. We also resample the photometric model, where the noise is estimated from the RMS of the background regions in the *HST* images.

For each realization of the model, we recalculate j_* in the individual and combined cases with the advantage of knowing the actual value of j_* from the input model j_{real}. The scatter in the deviations from this real value will give us an estimation of how good the measurement is in each case. This exercise quantifies the random error that would be obtained if a galaxy corresponding to the best-fitting model was observed with the same data mask, substructure, and similar noise
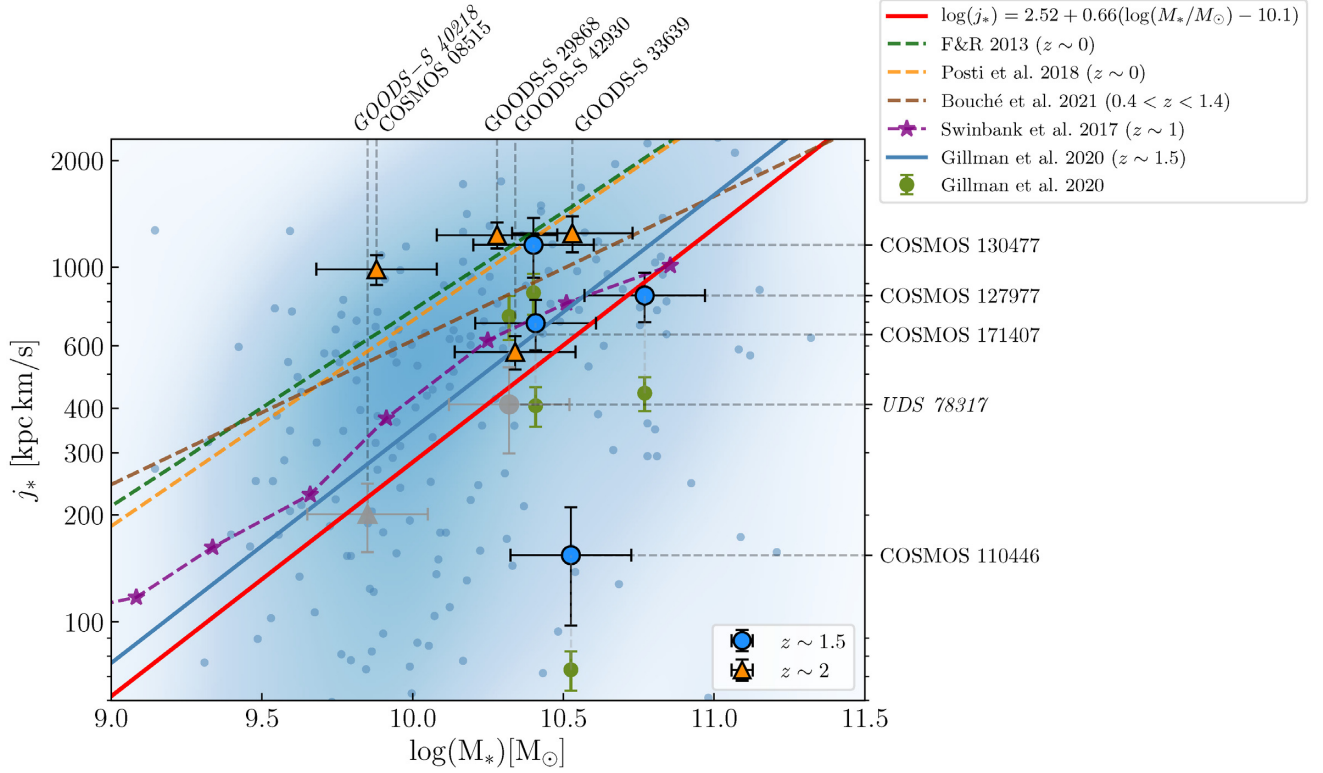
Figure 9. Stellar specific angular momentum j_* versus stellar mass M_* with the results from the combined analysis indicated by the blue circles ($z \sim 1.5$) and orange triangles ($z \sim 2$). The two grey data points correspond to the galaxies classified as mergers, so they are only shown for reference. Solid red line indicates the fit to the combined data of the eight disc galaxies in the form $\log(j_*) = \alpha + \beta(\log(M_*/M_\odot) - 10.1)$ for a fixed $\beta = 0.66$. Green and orange dashed lines correspond to the relations at $z \sim 0$ found for discs by Fall & Romanowsky (2013) and Posti et al. (2018), respectively. Purple stars correspond to the binned measurements from Swinbank et al. (2017) at $z \sim 1$ with MUSE and KMOS and brown dashed line corresponds to the intermediate redshift measurements ($0.4 < z < 1.4$) from Bouché et al. (2021). The blue solid line corresponds to the relation found for a large sample of seeing limited data (including non-discs) by Gillman et al. (2020) at $z \sim 1.5$ with the large scatter shown by the background blue dots and blue shading is the background density determined using a Gaussian kernel density estimation. The green points represent the j_* measurements of the five galaxies in our sample that overlap with the Gillman et al. (2020) measurements.

Table 4. Best-fitting parameters for our eight disc galaxies of the form $\log(j_*) = \alpha + \beta(\log(M_*/M_\odot) - 10.1)$. We show the results from the KGES sample (Gillman et al. 2020) in the third and fourth row for a direct comparison.

Data	β	α
Constrained fit ($\beta = 2/3$)	0.66	2.52 ± 0.11
Unconstrained fit	-0.49 ± 0.31	2.92 ± 0.11
KGES ($\beta = 2/3$)	0.66	2.6 ± 0.03
KGES unconstrained	0.53 ± 0.1	2.63 ± 0.04

levels. It also allows us to assess the systematic error levels in the methodology.

The systematic error in j_* for each galaxy is calculated from the median of the errors from the 100 realizations of the model. For the full sample, the average systematic errors are -4.4 per cent for the natural seeing data, -2.3 per cent for the adaptive optics data and -2.1 per cent in the combination. More importantly, by taking the standard deviation of the individual errors from the 100 realizations we obtain the error Δj_* for each galaxy as well as the errors in all parameters reported in Table 3. The mean percentage error for the measurements using natural seeing data is 49 per cent, in the case of adaptive optics 26.5 per cent and as for the combined resolutions it is 16 per cent as shown in Fig. 11. This clear improvement can be
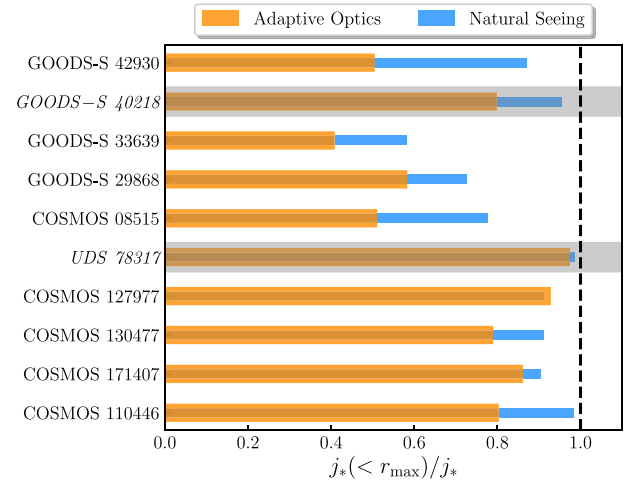

Figure 10. Angular momentum contained within the boundaries of the different data (extent of the velocity maps) in the combined analysis. The dashed vertical line represents the total stellar specific angular momentum j_*. The adaptive optics assisted data (orange) accounts only for about 72 per cent of j_*, whereas the natural seeing data accounts for about 86 per cent of j_*. Grey shades indicate the galaxies that cannot be treated as rotating disks.
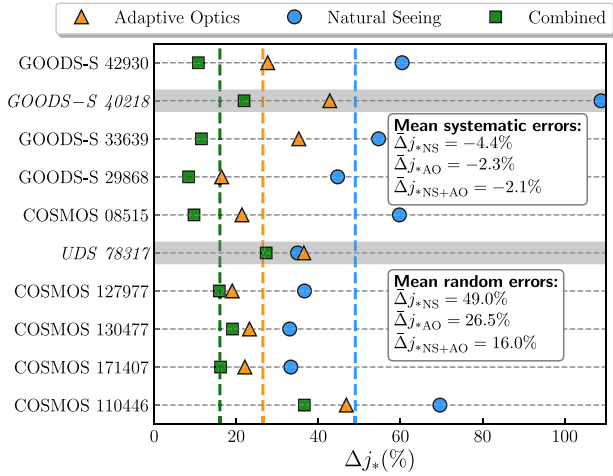
Figure 11. Uncertainties in j_* (per cent) obtained from resampling the best models in the individual and combined cases. The mean errors of the sample are indicated by the vertical dashed lines and are shown at the bottom right corner, while the mean systematic errors are shown in the top right.

explained by the better constraints imposed in the inner part of the rotation curves where the adaptive optics data is essential as well as the larger spatial extent of the combined data.

4.4 Geometrical parameters

We pay special attention in determining the position angle and inclination as they are critical quantities in the deprojection of the velocity field. In the case of the inclination, there is a well-known degeneracy between rotation velocity and inclination that arises from kinematic modelling alone (e.g. Begeman 1989; Epinat et al. 2010; Kamphuis et al. 2015; Bekiaris et al. 2016). In order to break this degeneracy, and noting that the uncertainty in the inclinations is one of the largest caveats in our analysis, we adopt a consistent approach to that of Swinbank et al. 2017 for relative comparison where we constrain the inclination i from the galaxies' surface brightness profiles as done by other kinematic codes (e.g. GalPaK^{3D}; Bouché et al. 2015). For axisymmetric disc-like galaxies, the axial ratio can be used to estimate the inclination (Holmberg 1946) as

$$\cos^2 i = \frac{q^2 - q_0^2}{1 - q_0^2}, \tag{6}$$

where $q = b/a$ is the observed axial ratio and $q_0 = c/a$ is the true axial ratio of an edge on system that depends on morphological type (Heidmann, Heidmann & de Vaucouleurs 1972; Fouque et al. 1990). In the thin-disc approximation $q_0 \approx 0$, so this relation reduces to $\cos i \approx b/a$, however, star-forming galaxies at high redshift show vertical dispersion (Law et al. 2007; Förster Schreiber et al. 2009) that corresponds to thick discs with $q_0 \approx 0.2$, so we adopt this value for consistency with previous studies at high redshift (e.g. Wisnioski 2012; Harrison et al. 2017; Gillman et al. 2020).

We compare the inclinations measured individually from photometry (i_{phot}) and from the kinematic modelling alone (i_{kin}), where we find that the kinematic modelling underestimates the inclinations for 8/10 of the galaxies in the sample as seen in Fig. 12. The values of i_{kin} of those eight galaxies are low $\leq 40°$, where the degeneracy with the velocity field (characterized by v_{flat}) escalates more rapidly as discussed by Bekiaris et al. (2016). This degeneracy leads to an increase on the v_{flat} parameter and thus an overall increase in
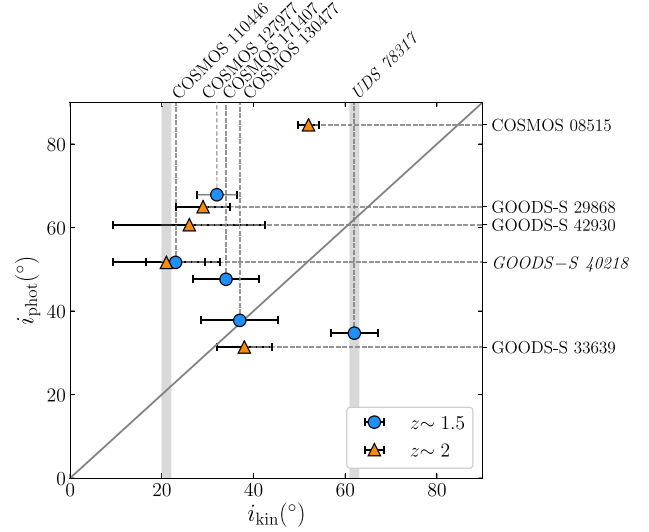

Figure 12. Direct comparison between the inclinations measured from the surface brightness profiles (i_{phot}) versus the measurements from the kinematic modelling alone (i_{kin}). Diagonal line represents the one-on-one correspondence.

the measurements of j_*. Besides the known degeneracy, such low inclinations deviate significantly from the mean expected inclination of disc galaxies given their random orientations in space. Following geometrical arguments, this mean expected value is $<\sin i> = 0.79$ (see the appendix of Law et al. 2009) which is consistent with the mean value of the photometric inclinations (and bootstrap errors) of our sample $<\sin i_{phot}> = 0.77 \pm 0.06$. On the other hand, the mean kinematic inclinations largely disagree with $<\sin i_{kin}> = 0.56 \pm 0.05$.

Moreover, the predictions on the Fall relation are significantly different when using the kinematic or photometric inclinations. If we used best-fitting parameters from the kinematic model alone (without constraining the inclination from photometry), we find a zero-point of 2.75 for the fixed power slope $\beta = 2/3$, which has a positive 0.23 offset with respect to the fit with the photometric inclinations. This experiment confirms the necessity of imposing constraints in the inclinations from the surface brightness profiles.

In the case of the position angle θ_{PA}, we used the values measured from the kinematic modelling since the equivelocity contours of the 'spider diagram' (e.g. the fourth column in Fig. 5) are indicative of a clear main axis. On the other hand, the position angle estimated from photometry depends on the light distribution which is more susceptible to global non-axisymmetric features within the disc (Palunas & Williams 2000). The θ_{PA} from kinematics is thus better constrained, especially in the combined case.

The misalignment between θ_{PA}^{kin} and θ_{PA}^{phot} can be a product of physical differences such as bright clumps in the continuum, the asymmetry between the stellar and gas distributions as well as complex morphologies due to mergers (Rodrigues et al. 2017). However, it can also be a product of the lack of precision in the deprojection of high redshift maps. We find that the galaxies that show the largest misalignment are the two mergers and the galaxy with large uncertainties (GOODS-S 33639) as indicated in Fig. 13, which is consistent with the disc-merger criteria discussed in Section 4.1. For the rest of the sample, there is an overall agreement in the position angles that supports the choice of using the photometric inclinations.
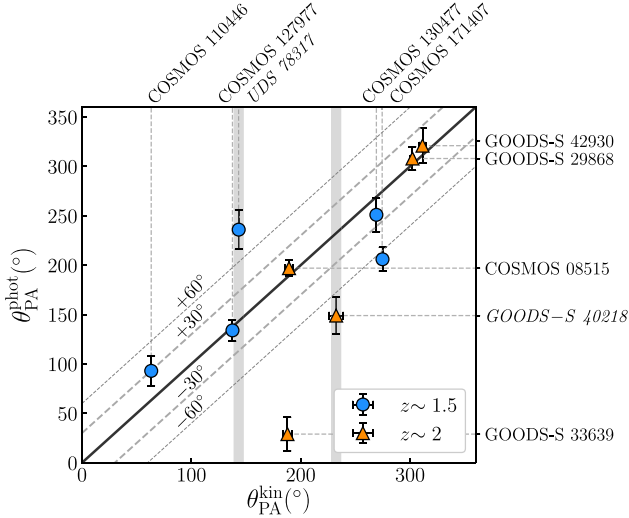
Figure 13. Comparison between the position angle obtained from photometry (y-axis) and kinematics (x-axis), where the measurements from kinematics are from the combined analysis (NS + AO). Dashed lines represent the regions with $\Delta\theta_{PA} = \pm 30°, \pm 60°$. The galaxies with large discrepancies are ones classified as mergers (*UDS 78317* and *GOODS-S 40218* indicated by the grey vertical lines) as well as GOODS-S 33639, which is highly uncertain in the photometric and kinematic fits.
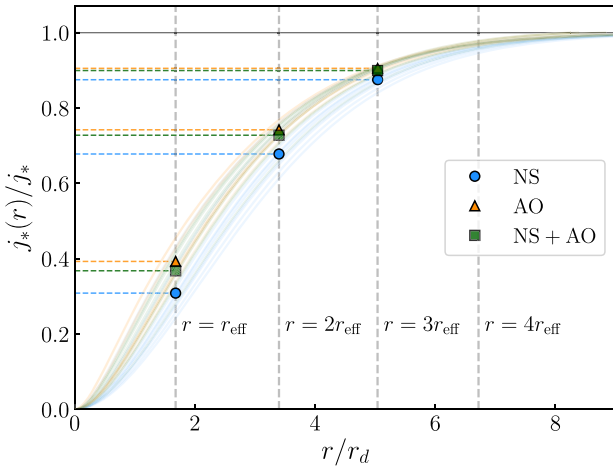

Figure 14. Cumulative profiles of $j_*(r)$ as a function of deprojected radius r_d for the full sample in both single and combined resolutions. Dashed vertical lines indicate the r_{eff}, $2r_{eff}$, $3r_{eff}$, $4r_{eff}$ distances from the galactic centre. The dots, triangles, and squares on top of these lines correspond to the mean $j_*(r)$ of the full sample to indicate the difference in the convergence from the different data types, which is significant at low radii.

4.5 Angular momentum convergence

Stellar specific angular momentum converges to an asymptotic value at large radii, with some notable differences between the different resolutions. A direct comparison of the convergence at different radii (namely $r = 1, 2$ and $3r_{eff}$) between the different data types shows that the measured j_* converges faster in the case of the high-resolution data as shown in Fig. 14. This result is expected since the rapidly growing rotation curves are better determined with the high-resolution data in the centre of the discs, whereas the flat part
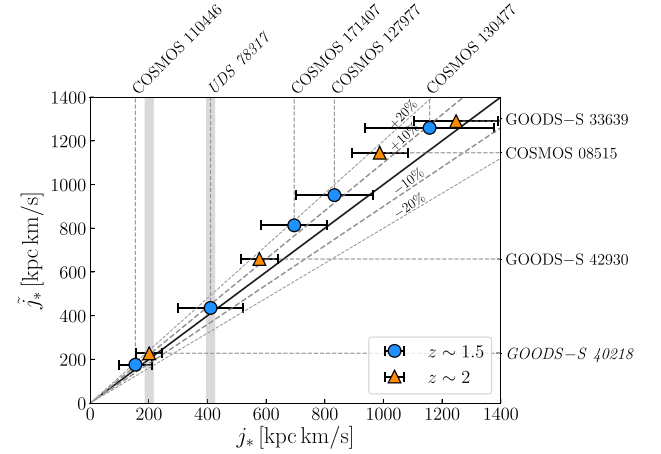
Figure 15. Stellar specific angular momentum from the approximation $\tilde{j}_* = k_n v_s r_{eff}$ with respect to the measurements from the combined analysis 'NS + AO', using the analytical expression of j_* in equation (2). The diagonal line indicates the perfect agreement $\tilde{j}_* = j_*$ which is followed by the whole sample at the 20 per cent level.

of the rotation curve is better determined with the seeing limited data where the effects of beam smearing are smaller.

Another consistent result that we find throughout the whole sample is that the approximation $\tilde{j}_*$ (equation 5), agrees within ~ 20 per cent with the total angular momentum value j_* measured from the best-fitting models in the combined analysis as in Fig. 15. This approximation relies on global variables that can be measured from low-resolution data such as the galaxy size and asymptotic velocity, hence natural seeing observations can provide a good estimation of the total angular momentum content of galaxies that are indeed disks as suggested by Romanowsky & Fall (2012).

4.6 Comparison with natural-seeing based results

We test the reliability of natural-seeing based estimations of j_* by comparing them with those from the combined analysis. In order to do that, we measure the ratio of both quantities as a function of disc scale length r_d as shown in Fig. 16, where no dependence on redshift or galaxy size was found.

We find that the NS-only measurements of j_* for the disc galaxies are within 10 per cent from the combined ones (with the exception of COSMOS 08515[8]), suggesting that if the galaxies are truly disks, then the natural seeing based estimations of j_* are reliable. However, in the case of the two galaxies classified as mergers, the discrepancy in the measurement is large (> 30 per cent), which shows how the poor determination of the real kinematic state of the galaxy (from low resolution) can lead to under- or overestimations of j_*. Even if the estimation of j_* from the combined analysis of those galaxies is also wrong (as the calculation is still done assuming an exponential disk with ordered rotation), the large difference between the two measurements could be used as an indicator of a complex kinematic state for future large samples.

In order to compare our results with other existing low-resolution studies and directly address the possible systematics associated with

---

[8]The large discrepancy is due to the dramatic difference between the values of v_{flat}, which is more prominently affected by beam smearing in the case of the NS fit (it has the lowest spatial resolution in the full sample with PSF FWHM = 0.966 arcsec).
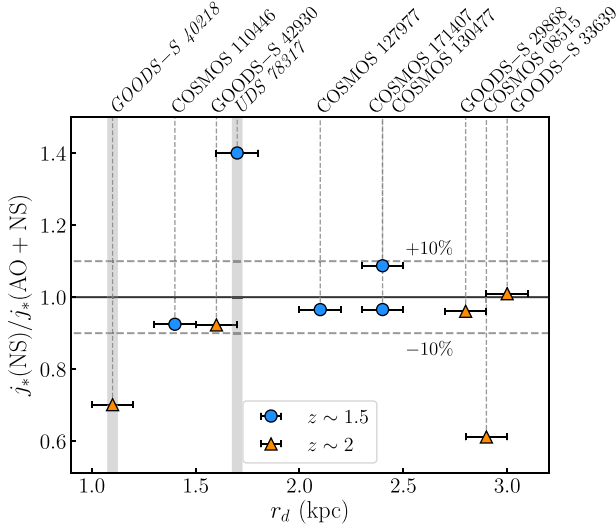
Figure 16. Ratio of the stellar specific angular momentum from the natural seeing (NS) sample and the value from the combined (NS + AO) analysis as a function of disc scale length r_d. Blue circles represent the sample at $z \sim 1.5$ and orange triangles the sample at $z \sim 2$. With the exception of COSMOS 08515, disc galaxies are in agreement within 10 per cent as shown by the dashed lines, whereas the two galaxies classified as mergers (*GOODS-S 40218* and *UDS 78317*) show a large disagreement. Additionally, there is no evidence for a strong dependence on the disc scale length or redshift.

our chosen method, we compare our individual measurements to those obtained for the KGES sample by Gillman et al. (2020) for the five galaxies at $z \sim 1.5$ that overlap with our sample. We compare their measurements with our natural-seeing only measurements (as well as the combined resolutions) as shown in Fig. 17. This is not a fully direct comparison since the functional form they used to measure j_* is different from ours but it allows to identify the systematic differences between the two approaches. The j_* values in Gillman et al. (2020) are obtained with the approximation $j_* \approx k_n v_s r_{\rm eff}$ (equation 5), where $r_{\rm eff}$ is measured from a Sérsic fit with GALFIT and v_s is obtained from a parametric model $v(r)$ that can rise or decline at large radii.[9] Since the KGES values of v_s are measured at $r = 2r_{\rm eff}$, where beam smearing effects are low, they are similar to our $v(r = 2r_{\rm eff})$ measurement at the 25 per cent level.

We find that the large differences in the galaxy-size measurement (shown in Table 5) directly translate into the large discrepancies of our measurements with the j_*(KGES) values. For the galaxies where our measurement of $r_{\rm eff}$ is significantly larger ($\Delta r_{\rm eff} > 75$ per cent) (COSMOS 110446, COSMOS 127977, and COSMOS 171407), the ratios in j_* are also significantly larger, whereas for the galaxies where the measurement of $r_{\rm eff}$ is smaller ($\Delta r_{\rm eff} < 50$ per cent) (COSMOS 130477 and *UDS 78317*), the j_* value is smaller as well.

The large difference in galaxy sizes can be attributed to the different surface brightness profiles $I(r)$ used in each case [Sérsic profile with varying $n = 0.2-8$ in Gillman et al. (2020) and exponential disc in our analysis] because the radius enclosing half of the light depends strongly on the power-law slope. This implies that an erroneous fit of the Sérsic index n, which could be caused by the low resolution of the *HST* maps and clumpy nature of these

[9]This parametric model of the rotation velocity is based on an exponential light profile, so it is characterized by the scale length of an exponential disc r_d (equation 10 in Freeman 1970).
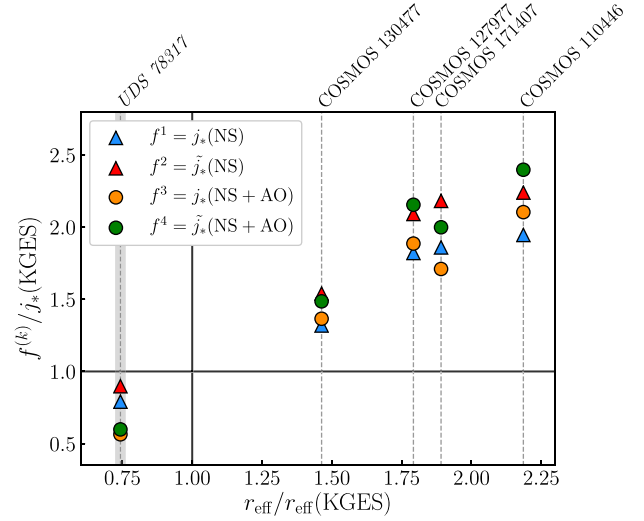
Figure 17. Comparison of our measurements of j_* with those from Gillman et al. (2020) for the five galaxies at $z \sim 1.5$ that overlap with our sample. We show the ratio $f^{(k)}/j_*$(KGES) (where $f^{(k)}$ is used to label the different types of measurements) with respect to the ratio of the effective radii measurements $r_{\rm eff}/r_{\rm eff}$(KGES) from Table 5. Blue (and red) triangles represent the total j_* (and approximated $\tilde{j}_*$) from the natural seeing 'NS' sample. Orange and green circles represent the combined measurements 'NS + AO'. Black solid lines indicate the regions, where the ratios are equal. The discrepancy in the measurement of $r_{\rm eff}$ translates directly into the discrepancy in the measurements of j_*.

Table 5. Effective (half-light) radius $r_{\rm eff}$ measurements from different studies. From left to right: Redshift, galaxy ID, $r_{\rm eff}$ obtained from the Sérsic's profile fit with the corresponding Sérsic index n, and our measurement from the exponential disc assumption which corresponds to $n = 1$. The five top rows correspond to the measurements from Gillman et al. (2020) of the KGES galaxies, where they follow the procedures of van der Wel et al. (2014) and the bottom five rows correspond to the measurements from Tacchella et al. (2015) of the SINS galaxies using the corresponding *HST H*-band images.

	Galaxy ID	$r_{\rm eff}$ (kpc) Gillman et al. (2020)	n	$r_{\rm eff}$ (kpc) (This work)
$z \sim 1.5$	COSMOS 110446	1.08	0.5	2.35
	COSMOS 171407	2.13	0.2	4.03
	COSMOS 130477	2.75	1.1	4.03
	COSMOS 127977	2.06	0.2	3.69
	UDS 78317	4.07	0.4	3.02
		Tacchella et al. (2015)		(This work)
$z \sim 2$	COSMOS 08515	2.2	0.5	4.9
	GOODS-S 29868	5.7	0.2	4.7
	GOODS-S 33639	3.6	0.6	5.0
	GOODS-S 40218	1.3	0.9	1.8
	GOODS-S 42930	1.7	1.3	2.7

galaxies, can lead to over or underestimations of the light profile as well as unrealistic values of $r_{\rm eff}$. For example, the steep gradient in SNR could bias the fit to smaller values of n (steep profile), and thus bias the fit to small values of $r_{\rm eff}$. In fact, some of the Sérsic fits, particularly those with $n \leq 0.2$, are at the limit of the fitting range and thus the estimations of the galaxy size are unreliable. In our analysis, we chose the $n = 1$ exponential profile, which has a shallower slope and thus contains a large fraction of the galaxy light in the outskirts, where the SNR of the data is low. For 6/10 galaxies,

the (average) radial surface brightness profile $\Sigma(r)$ has lower RMS residuals when using the exponential disc assumption as compared to the Sérsic fit as shown for each individual galaxy in Figs S1–S6 in the supplementary section.

The comparison to the results of the KGES sample also allows us to determine the intrinsic scatter in the j_* versus M_* relation. The rms scatter of the KGES seeing-limited sample is ∼0.56 dex, whereas for our eight discs we get ∼0.38 dex. Even though a sample of eight discs is not enough to make statistically significant predictions, we note that this is still a large scatter, suggesting that adding the high-resolution kinematic data does have a significant effect on it. This could indicate that the observed scatter found from low resolution studies is not related to systematic effects caused by poor resolution. Instead, this intrinsic scatter could be attributed to different mechanisms of retention and redistribution of angular momentum due to inflows and outflows, morphological differences, varied bulge-to-total fractions, and complex environmental conditions such as higher incidence of minor mergers and large gas accretion from cosmic filaments. In the local Universe, the rms scatter of the parametric relation of discs decreases to ≤0.2 dex (e.g. Romanowsky & Fall 2012; Obreschkow & Glazebrook 2014; Posti et al. 2018), pointing to the emerging of rotational support that assembles massive discs in the local Universe (Simons et al. 2017).

4.7 Effects of galaxy clumpiness

The precision of a direct pixel-by-pixel measurement of j_* from the actual data is limited by the number of pixels with useful information in $v(x, y)$ and $I(x, y)$ as well as their difference in pixel scales and spatial resolutions [this motivated the use of the analytical calculation from equation (2)]. However, it can be useful when trying to avoid bias from assumed models. In the case of the photometry, extensive star-formation activity in bright clumps (not necessarily massive) within the disks and a central bulge can affect the observed morphology from the *HST* maps which is not accounted for in the exponential disk assumption. We calculate the pixel-by-pixel stellar specific angular momentum of all galaxies as

$$j_* = \frac{\sum\limits_{i,j} v_{i,j} \Sigma_{i,j} r_{i,j}}{\sum\limits_{i,j} \Sigma_{i,j}}, \tag{7}$$

where i, j go through all the spatially-matched pixels in velocity and photometry. In order to quantify the effects of clumpiness as well as the chosen form of $I(x, y)$, we perform four separate experiments (the first three are shown in Fig. 18) that we explain in the following paragraphs.

(i) Using *HST* data instead of the $I(x,y)$ model: We take the measurement of j_* where $v(x, y)$ and $I(x, y)$ come from the best-fitting models and compare it to the measurement where $I(x, y)$ comes from the *HST* data directly. Galaxies COSMOS 110446, COSMOS 130477, COSMOS 127977, *UDS 78317*, and GOODS-S 29868 show a large difference at the > 40 per cent difference level (with j_* using the *HST* being higher), likely due to the multiple bright components located away from the centre in their *HST* maps. The difference in the rest of the galaxies is at the < 30 per cent level. The majority of the light coming from the bright regions comes from young stellar populations that ionize the surrounding gas, so it only represents a small fraction of the full mass content. Hence, if these clumps are young, then the assumption that light traces mass provides an upper bound in the systematic error which is at the 28 per cent level for the whole sample.
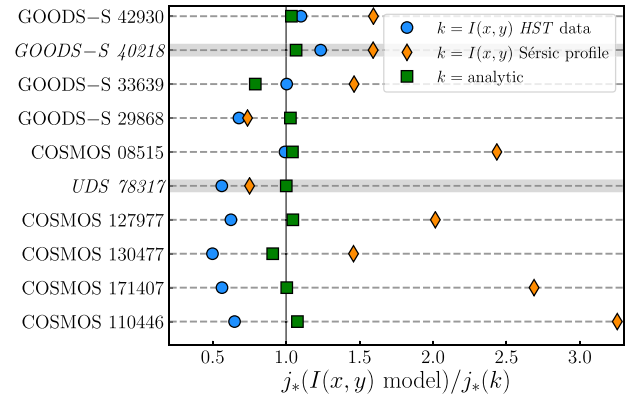

Figure 18. Fractional difference of the pixel-by-pixel measurement of j_* (equation 7) with respect to other measurements. (i) In blue circles, the difference with the estimation using the *HST* data instead of a model intensity profile $I(x, y)$ from where the $z \sim 1.5$ sample shows larger differences (> 30 per cent) due to clumpiness. (ii) Orange diamonds indicate the ratio with the estimation using a Sérsic profile with the fit parameters from Gillman et al. (2020) and Tacchella et al. (2015). The large ratios are directly related to the large difference in r_{eff} from the different surface brightness profiles shown in Table 5. (iii) In green squares, the difference with the analytical calculation (equation 2) which is always below the 30 per cent level.

(ii) Using a Sérsic profile (in 2D) instead of the exponential profile (in 2D): Another way to test the systematics associated with the choice of surface brightness profile is by using a Sérsic profile instead of the exponential disc. We use the best-fitting parameters from Gillman et al. (2020) and Tacchella et al. (2015) to create the $I(x, y)$ models from where we find large differences throughout the whole sample with the majority of the ratios being larger than unity (model $I(x, y)$ yields larger ratios than Sérsic profile $I(x, y)$) except for the merger UDS 78317 and GOODS-S 29868 which are the only galaxies where r_{eff} from the exponential disc fit is lower as seen in Table 5. In particular, we find dramatic differences at the >50 per cent level for six galaxies with COSMOS 110446 and COSMOS 171407 being the most extreme cases with ratios of 3.2 and 2.5, respectively. As mentioned in the previous subsection, despite the generalities that a Sérsic profile allows, steep gradients in the poorly constrained light profiles can lead to small values of n which translate to lower values of r_{eff} and thus underestimate the total value of j_*.

(iii) 2D approach versus 1D analytical calculation: In addition to testing the systematics associated with the assumed $I(x, y)$ model, we compare the pixel-by-pixel measurement with the estimation from the one-dimensional analytical expression in equation (2). We find a strong dependence in the disc scale length as the analytic calculation deviates significantly (> 10 per cent) in the case of COSMOS 08515 and GOODS-S 33639 which have the largest r_d (2.9 and 3 kpc, respectively). On the other hand, the galaxies where the difference in j_* is < 5 per cent (COSMOS 110446, *UDS 78317*, *GOODS-S 40218*, and GOODS-S 42930) are the galaxies with the lowest r_d with $r_d <$ 2 kpc. This scale dependence can be attributed to the error introduced by the discrete change in intensities (and velocities) from the pixel-by-pixel approach. This effect is stronger when r_d is large, since more pixels will have values that deviate more from the analytical expression which is more reliable since it depends only on r_d, r_{flat}, and v_{flat}.

(iv) Bulge and clumps contribution: We quantify the effect of adding a central bulge in the modelling that follows a Sérsic profile with $n = 4$ and a size of $r_{\mathrm{eff}} \sim 1$ kpc in our modelling. The choice of

this size is motivated by the findings of Fisher & Drory (2010) who estimate typical bulge sizes in the local Universe and the bulge-disc decomposition performed in Tacchella et al. (2015) on the SINS galaxies, where they find typical bulge sizes of ~1 kpc. We recalculate j_* with the modified mass distribution model while keeping the same velocity field information (since it is constrained by the multiple resolutions). We add the extra co-rotating component by varying the bulge-to-total ratio $(B/T)_*$ in the range of [0.1–0.5], noting that in the $(B/T)_*$ decomposition on J- and H-band *HST* images performed by Tacchella et al. (2015) on COSMOS 08515, GOODS-S 33639, *GOODS-S 40218*, and GOODS-S 42930, the bulge-to-total ratios were all in the range of [0–0.3].

For a constant mass-to-light ratio $(M/L)_*$, we find that the effect of the bulge is a decrease in the total measurement of j_*, in consistency with similar studies (e.g. Romanowsky & Fall 2012; Obreschkow & Glazebrook 2014). The effect is minimal at $(B/T)_* = 0.1$ with a small median decrease in j_* of ~ 2 per cent, and becomes more prominent at higher $(B/T)_*$, having the maximum effect at of $(B/T)_* = 0.5$ with a median decrease of 10 per cent in j_*. However, since the stellar populations in the bulge are different from those in the disk, then the $(M/L)_*$ in each component is different as well. In order to quantify this effect, we make use of the J- and H-band *HST* data at $z \sim 2$ used in Tacchella et al. (2015) (via private communication) to perform a colour analysis. Since J–H colours at $z \sim 2.2$ correspond to rest-frame u–g, we can use them as a proxy for stellar mass-to-light ratios $(M/L)_*$ based on colour–$(M/L)_*$ relations (Bell & de Jong 2001). From the radial colour profiles and colour maps, we find colour differences in the bulge and disc of $\Delta m \leq 0.3$ which translate to bulges that are ≤ 40 per cent more massive than the disc using the relations in Bell et al. (2003). This difference sets an upper bound of $\Delta j_* \lesssim 15$ per cent, and shows that galaxies with massive central bulges (higher mass-to-light ratios) have a lower content of stellar specific angular momentum.

A similar colour analysis of the galaxies with the most prominent clumps and high-quality *HST* multi-wavelength data (namely COSMOS 08515 and GOODS-S 29868) sets an upper bound on the effect of their bright clumps on the overall measurement of j_*. From the colour maps, we identify clumps that are bluer (younger) than the disc with a maximum difference of $\Delta(J - H) \sim -0.6$ that translates to a difference in mass-to-light ratio of $\Delta \log(M/L_*) \sim -0.3$. Thus, these clumps are 50 per cent less massive than their host discs so they contribute less to the mass profile of the galaxy. In parallel to the effect of the bulge, the effect of these young clumps in j_* is a slight decrease of 8 per cent for COSMOS 08515 (with two clumps) and 5 per cent for GOODS-S 29868 (one clump), where we have used clump sizes of $r \sim 1$ kpc from the *HST* broad-band imaging at their distance from the galaxy centre. The measurement of this effect is limited to the difference in mass profile as we did not include any extra kinematic components in the model. Besides its consistency with similar studies, this assumption is justified from the inspection of the velocity fields that show no significant differences in the regions where these clumps reside (they appear to co-rotate with the discs). For the rest of the sample, this contribution ($\Delta j_* \lesssim 10$ per cent) is expected to be of similar order, so it does not have a dramatic effect on the stellar specific angular momentum measurements in this work.

5 CONCLUSIONS

We have gathered and analysed a sample of 10 high-redshift ($z \sim 1.5$ and $z \sim 2$) galaxies that have IFS observations at high and low spatial resolution as well as near-infrared *HST* observations to measure their stellar specific angular momentum j_* content. This is the largest

sample to date with angular momentum measurements coming from the combination of adaptive optics assisted observations and their seeing limited counterparts. We summarize our findings as follows:

(i) We developed a code to combine and take advantage of the different capabilities of each data type (adaptive optics provides high resolution but low sensitivity and natural seeing provides low resolution but high sensitivity). In the '21/2D' modelling, we carefully apply the right convolution to each model cube and find the best model using a maximum likelihood technique. We successfully tested the kinematic code by simulating a sample of 10^3 mock galaxies with similar characteristics and running the code at different resolutions. Besides providing a sanity check for the code, it also confirmed that the combination of the different resolutions reduces the uncertainty in j_* as explained in Appendix A.

(ii) In order to increase SNR in two of the adaptive optics assisted datacubes, we employed different spatial smoothing methods and the median filter provided the best results. The signal was improved sufficiently so that Hα emission could be used to measure its emission line kinematics and the spatial resolution was kept high enough to improve that of seeing limited data.

(iii) We have measured the improvement in the uncertainties of j_* by resampling the models with a Monte Carlo approach. The mean uncertainties in the sample are 49 per cent in the natural seeing case, 26.5 per cent for adaptive optics and 16 per cent when combining the data sets. The improvement comes from a reduction in the effects of beam smearing and the accurate modelling of the rotation curves, which are expected to rise rapidly in the inner regions of disc galaxies (better determined with adaptive optics) and then flatten at large radii (better determined with the deeper seeing limited counterpart). The combination can thus improve the measurements of j_* that come from large seeing-limited surveys and will be more useful once large samples of adaptive optics assisted measurements are made with upcoming facilities such as *JWST* and next-generation ground-based IFUs.

(iv) Estimates of j_* from the natural seeing observations are reliable (within 10 per cent of the combined analysis) when the galaxies are confidently classified as discs. The only exception was galaxy COSMOS 08515 due to the very poor resolution in NS. This suggests that the reliability of the findings from large seeing limited surveys depends strongly on the accurate kinematic classification of the samples.

(v) Besides the measurement from the best-fitting models, we calculate the stellar specific angular momentum of all galaxies with a widely used approximation in terms of the rotation profile and size of the disk. This value labeled $\tilde{j}_*$ consistently agrees with the asymptotic angular momentum measurement obtained from the full modelling within 20 per cent.

(vi) A pixel-by-pixel measurement is subject to large systematic uncertainties due to resolution effects and pixel scales. A smooth profile assumption from an analytical calculation of $j_*(r)$ can reduce the effect of these systematics and its reliability depends on the choice of surface brightness and rotation velocity profiles. In particular, the size r_{eff} is a critical quantity in measuring j_* and depends strongly on the choice of $I(r)$.

(vii) We classify *GOODS-S 40218* and *UDS 78317* as mergers. The latter was previously defined as a rotating disc from natural seeing only studies but turned out to be a merger from the high-resolution observations, in accordance with Sweet et al. (2019). We find that two of the other systems (COSMOS 171407 and GOODS-S 33639) have complex Hα intensity and kinematic structures but insufficient to catalog them as mergers so we treat them as discs. The other six galaxies are classified as rotating discs.

(viii) We used the eight galaxies identified as discs to make a prediction on the Fall relation (j_* versus M_*). We find that our best fit with a constrained slope agrees with the findings of previous high-redshift studies within ∼0.3 dex. This is limited by the small number of galaxies in our current sample. A direct comparison to the relation found from a seeing limited sample at a similar redshift (Gillman et al. 2020 at $z \sim 1.5$) shows a minor offset, despite the differences in the methods used to measure j_* (different mass distributions and radial extents).

(ix) The scatter of our measurements in the Fall relation remains large (∼0.38 dex) even in the combined analysis in similarity with the 'NS-only' analysis of Gillman et al. (2020). The scatter is thus intrinsic and reflects diversity in galaxy assembly and complex morphology where stellar bulge-to-total ratios may play a more important role. In the local Universe, the scatter decreases to ∼0.2 pointing to the assembly of discs through rotational support.

In future work, we will apply the method introduced here on a larger sample from the seeing limited survey Förster Schreiber et al. (2009) with its adaptive optics counterparts from Förster Schreiber et al. (2018). This will expand the current combined analysis to a low-mass regime and will provide further constraints in the j_* versus M_* relation from multiresolution measurements of j_*.

ACKNOWLEDGEMENTS

DATA AVAILABILITY

The data underlying this article will be shared on reasonable request to the corresponding author.

REFERENCES

Airy G. B., 1835, Trans. Cambridge Phil. Soc., 5, 283
Astropy Collaboration, 2013, A&A, 558, A33
Avila R. J., 2017, Advanced Camera for Surveys Instrument Handbook for Cycle 25 v. 16.0
Bacon R. et al., 2010, in McLean I. S., Ramsay S. K., Takami H., eds, Proc. SPIE Conf. Ser. Vol. 7735, Ground-based and Airborne Instrumentation for Astronomy III. SPIE, Bellingham, p. 773508
Bassett R. et al., 2014, MNRAS, 442, 3206
Begeman K. G., 1989, A&A, 223, 47
Bekiaris G., Glazebrook K., Fluke C. J., Abraham R., 2016, MNRAS, 455, 754
Bellocchi E., Arribas S., Colina L., 2012, A&A, 542, A54
Bell E. F., de Jong R. S., 2001, ApJ, 550, 212
Bell E. F., McIntosh D. H., Katz N., Weinberg M. D., 2003, ApJS, 149, 289
Bezanson R. et al., 2018, ApJ, 858, 60
Blumenthal G. R., Faber S., Primack J. R., Rees M. J., 1984, Nature, 311, 517
Boissier S., Prantzos N., Boselli A., Gavazzi G., 2003, MNRAS, 346, 1215
Bouché N. et al., 2007, ApJ, 671, 303
Bouché N., Carfantan H., Schroetter I., Michel-Dansac L., Contini T., 2015, AJ, 150, 92
Bouché N. F. et al., 2021, A&A, 654, A49
Burkert A. et al., 2016, ApJ, 826, 214
Carignan C., Chemin L., Huchtmeier W. K., Lockman F. J., 2006, ApJ, 641, L109
Catelan P., Theuns T., 1996a, MNRAS, 282, 436
Catelan P., Theuns T., 1996b, MNRAS, 282, 455
Catinella B., Giovanelli R., Haynes M. P., 2006, ApJ, 640, 751
Conselice C. J., Bershady M. A., Jangren A., 2000, ApJ, 529, 886
Contini T. et al., 2016, A&A, 591, A49
Cortese L. et al., 2016, MNRAS, 463, 170
Cresci G. et al., 2009, ApJ, 697, 115
Davies R., Kasper M., 2012, ARA&A, 50, 305
de Blok W. J. G., Walter F., Brinks E., Trachternach C., Oh S. H., Kennicutt R. C. J., 2008, AJ, 136, 2648
Decarli R. et al., 2019, ApJ, 882, 138
Dekel A., Burkert A., 2014, MNRAS, 438, 1870
Dekel A., Sari R., Ceverino D., 2009, ApJ, 703, 785
di Teodoro E. M., Fraternali F., 2015, MNRAS, 451, 3021
Eisenhauer F. et al., 2003, in Iye M., Moorwood A. F. M., eds, Proc. SPIE Conf. Ser. Vol. 4841, Instrument Design and Performance for Optical/Infrared Ground-based Telescopes. SPIE, Bellingham, p. 1548
Elmegreen D. M., Elmegreen B. G., Rubin D. S., Schaffer M. A., 2005, ApJ, 631, 85
Epinat B., Amram P., Balkowski C., Marcelin M., 2010, MNRAS, 401, 2113
Epinat B. et al., 2012, A&A, 539, A92
Fall S. M., 1983, in Athanassoula E., ed., Proc. IAU Symp. 100, Internal Kinematics and Dynamics of Galaxies. Kluwer, Dordrecht, p. 391
Fall S. M., Efstathiou G., 1980, MNRAS, 193, 189
Fall S. M., Romanowsky A. J., 2013, ApJ, 769, L26
Fall S. M., Romanowsky A. J., 2018, ApJ, 868, 133
Fisher D. B., Drory N., 2010, ApJ, 716, 942
Fisher D. B. et al., 2017, MNRAS, 464, 491
Foreman-Mackey D., Hogg D. W., Lang D., Goodman J., 2013, PASP, 125, 306
Förster Schreiber N. M. et al., 2009, ApJ, 706, 1364
Förster Schreiber N. M. et al., 2018, ApJS, 238, 21
Fouque P., Bottinelli L., Gouguenheim L., Paturel G., 1990, ApJ, 349, 1
Freeman K. C., 1970, ApJ, 160, 811
Genzel R. et al., 2006, Nature, 442, 786
Genzel R. et al., 2008, ApJ, 687, 59
Giavalisco M. et al., 2004, ApJ, 600, L93
Gillman S. et al., 2019, MNRAS, 486, 175
Gillman S. et al., 2020, MNRAS, 492, 1492
Glazebrook K., 2013, Publ. Astron. Soc. Aust., 30, e056
Glazebrook K., Ellis R., Santiago B., Griffiths R., 1995, MNRAS, 275, L19

Guérou A. et al., 2017, A&A, 608, A5

Harrison C. M. et al., 2017, MNRAS, 467, 1965

Heidmann J., Heidmann N., de Vaucouleurs G., 1972, MmRAS, 75, 85

Holmberg E., 1946, Meddelanden fran Lunds Astronomiska Observatorium Serie II, 117, 3

Hubble E., 1926, Contributions from the Mount Wilson Observatory / Carnegie Institution of Washington, 324, 1

Hunter J. D., 2007, Comput. Sci. Eng., 9, 90

Józsa G. I. G., Kenn F., Klein U., Oosterloo T. A., 2007, A&A, 468, 731

Kamphuis P., Józsa G. I. G., Oh S.- H., Spekkens K., Urbancic N., Serra P., Koribalski B. S., Dettmar R. J., 2015, MNRAS, 452, 3139

Koekemoer A. M. et al., 2011, ApJS, 197, 36

Krajnović D., Cappellari M., de Zeeuw P. T., Copin Y., 2006, MNRAS, 366, 787

Larkin J. et al., 2006, Proc. SPIE Conf. Ser. Vol. 6269, Ground-based and Airborne Instrumentation for Astronomy. SPIE, Bellingham, p. 62691A

Lawrence A. et al., 2007, MNRAS, 379, 1599

Law D. R., Steidel C. C., Erb D. K., Larkin J. E., Pettini M., Shapley A. E., Wright S. A., 2007, ApJ, 669, 929

Law D. R., Steidel C. C., Erb D. K., Larkin J. E., Pettini M., Shapley A. E., Wright S. A., 2009, ApJ, 697, 2057

Liao S., Gao L., Frenk C. S., Guo Q., Wang J., 2017, MNRAS, 470, 2262

Livermore R. C. et al., 2015, MNRAS, 450, 1812

Madau P., Dickinson M., 2014, ARA&A, 52, 415

Marasco A., Fraternali F., Posti L., Ijtsma M., Di Teodoro E. M., Oosterloo T., 2019, A&A, 621, L6

Markwardt C. B., 2009, in Bohlender D. A., Durand D., Dowler P., eds, ASP Conf. Ser. Vol. 411, Astronomical Data Analysis Software and Systems XVIII. Astron. Soc. Pac., San Francisco, p. 251

Mieda E., 2015, PhD thesis, Univ. Toronto

Mobasher B. et al., 2015, ApJ, 808, 101

Moffat A. F. J., 1969, A&A, 3, 455

Mowla L. A. et al., 2019, ApJ, 880, 57

Mo H. J., Mao S., White S. D. M., 1998, MNRAS, 295, 319

Naab T., Ostriker J. P., 2017, ARA&A, 55, 59

Obreschkow D., Glazebrook K., 2014, ApJ, 784, 26

Obreschkow D. et al., 2015, ApJ, 815, 97

Palunas P., Williams T. B., 2000, AJ, 120, 2884

Peebles P. J. E., 1969, ApJ, 155, 393

Pichon C., Pogosyan D., Kimm T., Slyz A., Devriendt J., Dubois Y., 2011, MNRAS, 418, 2493

Posti L., Fraternali F., Di Teodoro E. M., Pezzulli G., 2018, A&A, 612, L6

Rodrigues M., Hammer F., Flores H., Puech M., Athanassoula E., 2017, MNRAS, 465, 1157

Romanowsky A. J., Fall S. M., 2012, ApJS, 203, 17

Scoville N. et al., 2007, ApJS, 172, 1

Sellwood J. A., Spekkens K., 2015, preprint (arXiv:1509.07120)

Sharples R. et al., 2013, Messenger, 151, 21

Simons R. C. et al., 2017, ApJ, 843, 46

Simons R. C. et al., 2019, ApJ, 874, 59

Simon J. D., Bolatto A. D., Leroy A., Blitz L., 2003, ApJ, 596, 957

Stott J. P. et al., 2016, MNRAS, 457, 1888

Sweet S. M. et al., 2019, MNRAS, 485, 5700

Swinbank A. M. et al., 2017, MNRAS, 467, 3140

Szomoru D., Franx M., Bouwens R. J., van Dokkum P. G., Labbé I., Illingworth G. D., Trenti M., 2011, ApJ, 735, L22

Tacchella S. et al., 2015, ApJ, 802, 101

Tacchella S., Dekel A., Carollo C. M., Ceverino D., DeGraf C., Lapiner S., Mand elker N., Primack Joel R., 2016, MNRAS, 457, 2790

Tacconi L. J. et al., 2013, ApJ, 768, 74

Teklu A., Remus R., Dolag K., Beck A., Burkert A., Schmidt A., Schulze F., Steinborn L., 2015, ApJ, 812, 29

Teuben P. J., 2004, in Ochsenbein F., Allen M. G., Egret D., eds, ASP Conf. Ser. Vol. 314, Astronomical Data Analysis Software and Systems (ADASS) XIII. Astron. Soc. Pac., San Francisco, p. 621

Tiley A. L. et al., 2019a, MNRAS, 482, 2166

Tiley A. L. et al., 2019b, MNRAS, 485, 934

Tiley A. L. et al., 2021, MNRAS, 506, 323

Tully R. B., Fisher J. R., 1977, A&A, 500, 105

van de Hulst H. C., Raimond E., van Woerden H., 1957, Bull. Astron. Inst. Netherlands, 14, 1

van den Bosch F. C., 1998, ApJ, 507, 601

van der Hulst J. M., Terlouw J. P., Begeman K. G., Zwitser W., Roelfsema P. R., 1992, in Worrall D. M., Biemesderfer C., Barnes J., eds, ASP Conf. Ser. Vol. 25, Astronomical Data Analysis Software and Systems I. Astron. Soc. Pac., San Francisco, p. 131

van der Velden E., 2020, J. Open Source Softw., 5, 2004

van der Walt S., Colbert S. C., Varoquaux G., 2011, Comput. Sci. Eng., 13, 22

van der Wel A. et al., 2014, ApJ, 788, 28

Ventou E. et al., 2017, A&A, 608, A9

Ventou E. et al., 2019, A&A, 631, A87

Virtanen P. et al., 2020, Nat. Meth., 17, 261

Wechsler R. H., Tinker J. L., 2018, ARA&A, 56, 435

Whitaker K. E. et al., 2019, ApJS, 244, 16

Wisnioski E. et al., 2015, ApJ, 799, 209

Wisnioski E. et al., 2019, ApJ, 886, 124

Wisnioski E., 2012, PhD thesis, Swinburne Univ. Technology

Zasov A. V., Saburova A. S., Khoperskov A. V., Khoperskov S. A., 2017, Physics Uspekhi, 60, 3

SUPPORTING INFORMATION

Supplementary data are available at *MNRAS* online.

Figure S1 Main results of galaxy COSMOS 110446 at the individual and combined resolutions.

Figure S2 Analysis of COSMOS 171407 (top) and COSMOS 130477 (bottom).

Figure S3 Analysis of COSMOS 127977 (top) and *UDS 78317* (bottom).

Figure S4 Analysis of COS4 08515 (top) and GOODS-S 29868 (bottom).

Figure S5 Analysis of GOODS-S 33639 (top) and *GOODS-S 40218* (bottom).

Figure S6 Analysis of GOODS-S 42930.

Please note: Oxford University Press is not responsible for the content or functionality of any supporting materials supplied by the authors. Any queries (other than missing material) should be directed to the corresponding author for the article.

APPENDIX A: KINEMATIC FITTING CODE

We developed a fitting code based on a maximum likelihood estimation with EMCEE[10] (Foreman-Mackey et al. 2013) that takes the velocity fields from two different data sets of the same galaxy and finds the best kinematic model. As mentioned in the main text, the two data sets can have different spatial resolutions, radial extents, alignments and pixel scales. Additionally, the code can also find the best fit from individual data.

The deprojected velocity models are built following Obreschkow & Glazebrook (2014) (Appendix B) where the parameters to fit are position angle θ_{PA}, inclination i, kinematic centre coordinates (x_0, y_0), asymptotic velocity v_{flat} and characteristic radius of the rotation curve r_{flat}. The deprojected velocity model is obtained by multiplying the circular velocity model $v_c(x, y)$ by a deprojection function in each pixel as

$$v(x, y) = \mathcal{C}(x, y)v_c(x, y), \tag{A1}$$

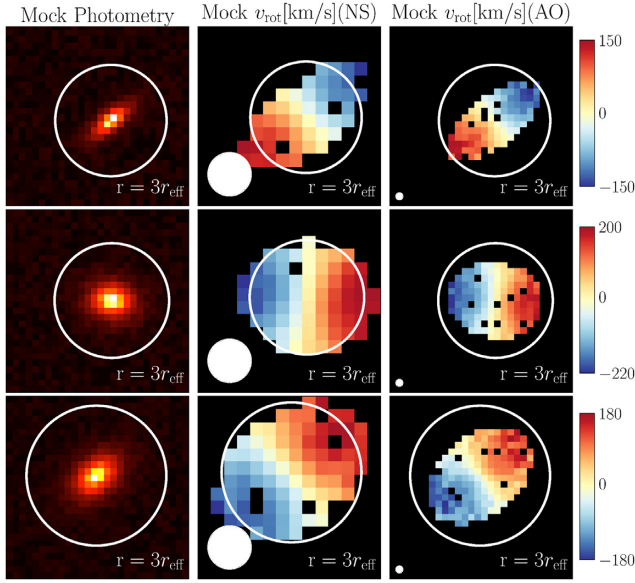[10] https://emcee.readthedocs.io/en/stable/

Figure A1. Example of three of the 10^3 mock galaxies used to test the kinematic code. Each row shows a simulated mock galaxy in photometry and the kinematics from the natural seeing and adaptive optics resolutions respectively. White empty circles represent the $r = 3r_{eff}$ boundary to show the extent of the data while the filled circles represent the size of the PSF.
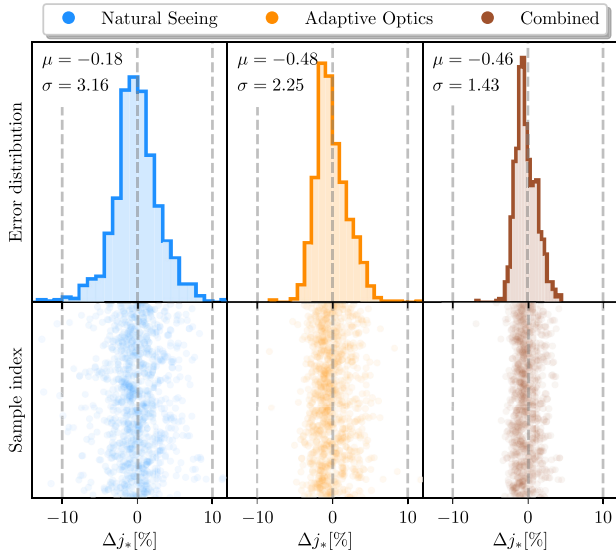

Figure A2. Results from the test of the kinematic code when applied to the 10^3 mock galaxies. Bottom panels: Fractional error of the obtained value of j_* with respect to the real input value j_{real} for each of the mock galaxies. Top panels: Histograms representing the spread in errors, where μ is the systematic fractional error and σ the spread in the random errors.

where $\mathcal{C}(x, y)$ is called the deprojection factor and is calculated as

$$\mathcal{C}(x, y) = \frac{\sin i}{\sqrt{1 + (y'/x')^2}} \, \text{sgn}(x'), \quad (A2)$$

with x' and y' the face-on coordinates that are computed from the parameters position angle θ_{PA}, inclination i and kinematic centre (x_0, y_0) as

$$x' = \cos \theta_{PA}(x - x_0) + \sin \theta_{PA}(y - y_0), \quad (A3)$$

$$y' = \frac{\cos \theta_{PA}(y - y_0) - \sin \theta_{PA}(x - x_0)}{\cos i}. \quad (A4)$$

After the deprojected velocity model is created, it is masked so that it matches the input velocity field in each pixel and it is then used to create a model datacube. The position of the model emission line is drawn from the velocity model and the line intensity is given by an input surface mass density model characterized by the size of the galaxy r_d. The width of the line is modelled according to the instrument spectral resolution. The model datacube is then convolved with the data PSF accordingly (Airy Disc + Moffat kernels in the adaptive optics case and a Gaussian kernel for natural seeing) and the velocity maps are then extracted from the convolved cubes.

The best-fitting model is obtained from minimizing the negative log-likelihood function (which corresponds to maximizing the log-likelihood), using the two input velocity fields and the two model velocity fields. The initial guess for the position angle is estimated using PAFIT[11] and the initial guess of the kinematic centre is estimated from a visual inspection of the peak in the Hα intensity maps. The best-fitting parameters from the probability distribution are calculated as the median of the marginalized parameters in the last 100 steps of the MCMC run which corresponds to the maximum of the likelihood function in the hyperspace of parameters.

In the case of fitting to a single resolution, the χ^2 used in the likelihood estimation is drawn from the individual fit. In the case of the combined analysis, where the data at both resolutions is used, the χ^2 is the sum of the two different contributions from the two data sets:

$$\chi^2 = \underbrace{\sum_{i,j} \frac{(v_{i,j} - \tilde{v}_{i,j})^2}{\sigma_{i,j}^2}}_{\chi^2_{NS}} + \underbrace{\sum_{k,l} \frac{(v_{k,l} - \tilde{v}_{k,l})^2}{\sigma_{k,l}^2}}_{\chi^2_{AO}}, \quad (A5)$$

where i, j represent the coordinates in the natural seeing data and k, l represent the coordinates in the adaptive optics data, which do not need to be correlated since each model is fit separately.

In order to verify the efficacy of the code and quantify the improvement when doing the combined analysis, we simulated a sample of 10^3 mock galaxies that resemble our real sample. The mock galaxies are built by creating a perfect intensity cube and photometric map with different values of position angle ($0° \leq \theta_{PA} \leq 360°$), inclination ($20° \leq i \leq 90°$), galaxy centre $[x_0, y_0]$ at a random distance of $d \leq 3$ pixels from the centre, asymptotic velocity ($80 \leq v_{flat} \leq 320$ km s^{-1}), characteristic radius of the rotation curve ($1 \leq r_{flat} \leq 2.52$ kpc) and disc scale length ($1.5 \leq r_d \leq 2.52$ kpc). After extracting the velocity field we introduced Gaussian noise at the level of the real data but also instrumental limitations and loss of random pixels due to signal-to-noise ratio. Fig. A1 shows an example of three of these mock galaxies.

For each mock galaxy, we ran the fitting code in the three cases (natural seeing only, adaptive optics only and combined resolutions). In each case, we obtain a best-fitting value of specific angular momentum $j_{*, fit}$ which can be compared to the input value of the model $j_{*, real}$.

The first notable result is that the spread in the percentage error $\Delta j_* = 100 \times (j_{*, fit} - j_{*, real})/j_{*, real}$ is largest in the natural seeing only case with $\sigma = 3.2$ per cent, followed by the adaptive optics only case with $\sigma = 2.3$ per cent. In the case of the combined analysis, the spread in the percentage error is the lowest with $\sigma = 1.4$ per cent,
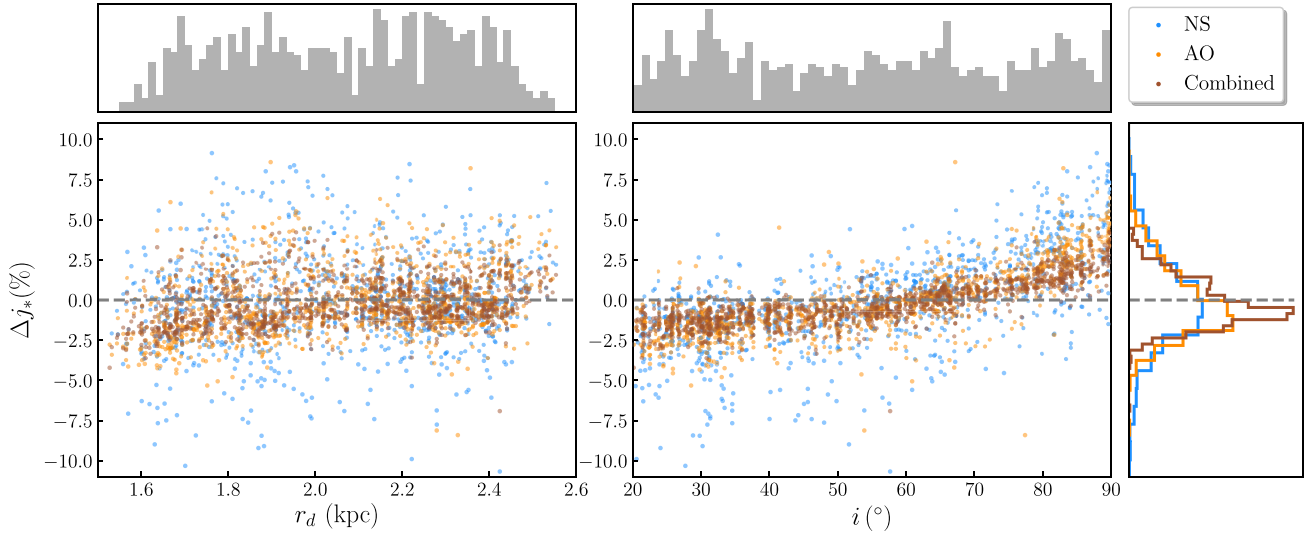
[11] http://www-astro.physics.ox.ac.uk/~mxc/software/#pafit

Figure A3. Distribution of errors (per cent) from the simulations against the input disc scale length r_d and inclination i. Top panels show the near-uniform distribution of simulated values of r_d and i which were chosen to be in the range $1.5 \leq r_d \leq 2.52$ kpc and $20° \leq i \leq 90°$, respectively. Right-hand panel shows the histograms of the individual and combined analysis showing only a small negative systematic offset (~ 1 per cent) towards lower values of j_*.

as shown by the histograms in Fig. A2. Additionally, the mean systematic percentage error μ in each case is low (-0.2 per cent, -0.5 per cent, and -0.5 per cent, respectively) that illustrates the robustness of the code.

Additionally, we test the accuracy of the angular momentum measurement as a function of the input size and inclination of the mock galaxies by comparing the percentage errors $\Delta j_* = 100 \times (j_{*,\,\mathrm{fit}} - j_{*,\,\mathrm{real}})/j_{*,\,\mathrm{real}}$ with the input values of r_d and i as shown in Fig. A3. We find no significant dependence on disk scale length as the mean trend is within 2.5 per cent and the rms is of a similar order for all three cases. As expected, the uncertainty decreases slightly towards larger radii since larger discs have a higher number of useful pixels in the fit, thus the error is smaller. The effect of disc inclination is noticeable for high and low values of i corresponding to near edge-on and near face-on projections of the disk. In the former, the small

number of useful pixels in the deprojection affects the accuracy of the fit and in the latter, the line of sight velocities are low and closer to the noise values. These effects are particularly noticeable in the NS case given the large pixel scales where Δj_* can be up to ~ 10 per cent in some cases. However, given the conservative range that we used for the inclinations ($i > 20°$) and the lack of additional features such as bulges or non-symmetrical clumps in the mock photometry maps, the inclinations found by the code are in very good agreement with the input values so these effects are small and merit special attention only when individual galaxies have very low inclinations at low resolution.

This paper has been typeset from a TEX/LATEX file prepared by the author.